Anderson orthogonality in the dynamics after a local quantum quench

Wolfgang Münder,[1] Andreas Weichselbaum,[1] Moshe Goldstein,[2] Yuval Gefen,[3] and Jan von Delft[1]

[1]*Physics Department, Arnold Sommerfeld Center for Theoretical Physics, and Center for NanoScience, Ludwig-Maximilians-Universität, Theresienstrasse 37, 80333 Munich, Germany*

[2]*Department of Physics, Yale University, 217 Prospect Street, New Haven, Connecticut 06520, USA*

[3]*Department of Condensed Matter Physics, The Weizmann Institute of Science, Rehovot 76100, Israel*

(Received 3 September 2011; revised manuscript received 17 May 2012; published 4 June 2012)

We present a systematic study of the role of Anderson orthogonality for the dynamics after a quantum quench in quantum impurity models, using the numerical renormalization group. As shown by Anderson in 1967, the scattering phase shifts of the single-particle wave functions constituting the Fermi sea have to adjust in response to the sudden change in the local parameters of the Hamiltonian, causing the initial and final ground states to be orthogonal. This so-called Anderson orthogonality catastrophe also influences dynamical properties, such as spectral functions. Their low-frequency behavior shows nontrivial power laws, with exponents that can be understood using a generalization of simple arguments introduced by Hopfield and others for the x-ray edge singularity problem. The goal of this work is to formulate these generalized rules as well as to numerically illustrate them for quantum quenches in impurity models involving local interactions. As a simple yet instructive example, we use the interacting resonant level model as testing ground for our generalized Hopfield rule. We then analyze a model exhibiting population switching between two dot levels as a function of gate voltage, probed by a local Coulomb interaction with an additional lead serving as charge sensor. We confirm a recent prediction that charge sensing can induce a quantum phase transition for this system, causing the population switch to become abrupt. We elucidate the role of Anderson orthogonality for this effect by explicitly calculating the relevant orthogonality exponents.

DOI: 10.1103/PhysRevB.85.235104 PACS number(s): 71.27.+a, 73.21.La, 72.10.Fk, 05.10.Cc

I. INTRODUCTION

The Anderson orthogonality (AO) catastrophe[1,2] refers to the response of a Fermi sea to a change in a local scattering potential, described, say, by a change in Hamiltonian from $\hat{H}_\mathrm{i}$ to $\hat{H}_\mathrm{f}$. Such a change induces changes in the scattering phase shifts of all single-particle wave functions. This causes the initial ground state $|G_\mathrm{i}\rangle$ of $\hat{H}_\mathrm{i}$ and the final ground state $|G_\mathrm{f}\rangle$ of $\hat{H}_\mathrm{f}$, both describing a filled Fermi sea but with respect to different single-particle wave functions, to be orthogonal in the thermodynamic limit, even if the changes in the single-particle wave functions are minute. The overlap of the respective ground states scales as[1–3]

$$|\langle G_\mathrm{i}|G_\mathrm{f}\rangle| \sim N^{-\frac{1}{2}\Delta_\mathrm{AO}^2}, \tag{1}$$

where N is the number of particles in the system, and the exponent Δ_AO characterizes the degree of orthogonality.

AO underlies the physics of numerous dynamical phenomena such as the Fermi edge singularity,[3–6] the Altshuler-Aronov zero bias anomaly[7] in disordered conductors, tunneling in metals[8] and into strongly interacting Luttinger liquids,[9–13] and optical absorption involving a Kondo exciton,[14–16] where photon absorption induces a local quantum quench, to name but a few. Recently, AO has also been evoked[17,18] in an analysis of *population switching* (PS) in quantum dots (the fact that the population of individual levels of a quantum dot may vary nonmonotonically with the gate voltage), and was argued to lead, under certain conditions involving a local Coulomb interaction with a nearby charge sensor, to a quantum phase transition.

One of the goals of the present work is to analyze the latter prediction in quantitative detail. Another is to generalize arguments that were given in Refs. 14–16, for the role of AO for spectral functions of the excitonic Anderson model, to related models with a similar structure. Thus we present a systematic study of the role of Anderson orthogonality for the dynamics after a quantum quench in quantum impurity models involving local interactions, using the numerical renormalization group (NRG).[19,20] We thereby extend a recent study,[21] which showed how Δ_AO can be calculated very accurately (with errors below 1%) by using NRG to directly evaluate overlaps such as $\langle G_\mathrm{i}|G_\mathrm{f}\rangle$, to the domain of dynamical quantities.

The spectral functions that characterize a local quantum quench typically show power-law behavior, $\sim\omega^{-1+2\eta}$, in the limit of small frequencies, where η typically depends on Δ_AO.[3–6] For the case of the x-ray edge singularity, Hopfield[5] gave a simple argument to explain the relation between Δ_AO and η. We frame Hopfield's argument in a more general setting and numerically illustrate the validity of the resulting generalized Hopfield rule [see Eq. (29) below] for several nontrivial models. In particular, we also analyze how this power-law behavior is modified at low frequencies when one adds to the Hamiltonian an extra tunneling term that describes transitions between the Hilbert spaces characterizing the "initial" and "final" configurations. This effect plays a crucial role in understanding the above mentioned quantum phase transition for population switching.

The paper is organized as follows. In Sec. II, we review various consequences of AO in different but related settings, and formulate the above mentioned generalization of Hopfield's rule. In Sec. III, we illustrate this rule for the spinless interacting resonant level model (IRLM), involving a single localized level interacting with the Fermi sea of a single lead. We consider this model without and with tunneling and study a quantum quench of the energy of its local level, focusing on signatures of AO in each case. Finally, in Secs. IV

and V, we discuss population switching without and with a charge sensor, respectively, confirming that if the sensor is sufficiently strongly coupled, AO indeed does cause population switching to become a sharp quantum phase transition. Section VI offers concluding remarks and outlines prospective applications of the present analysis.

II. VARIOUS CONSEQUENCES OF ANDERSON ORTHOGONALITY

In this section, we review various consequences of AO, in different but related settings. We begin by recalling two well-known facts: first, the relation between the exponent $\Delta_{\rm AO}$ and the charge that is displaced due to the quantum quench, $\Delta_{\rm ch}$, and second, the role of $\Delta_{\rm AO}$ in determining the asymptotic long-time power-law decay of correlation functions $\mathcal{G}_X(t)$ involving an operator $\hat{X}^\dagger$ that connects the initial and final ground states.

Then we consider the spectral function $\mathcal{A}_X(\omega)$ associated with $\mathcal{G}_X(t)$, which correspondingly shows asymptotic power-law behavior, $\sim\omega^{-1+2\eta}$, for small frequencies, where the exponent η depends on $\Delta_{\rm AO}$. We recall and generalize an argument due to Hopfield, that extends the relation between η and $\Delta_{\rm AO}$ to composite local operators. Finally, we recapitulate how all these quantities can be calculated using NRG.

For simplicity, we assume in most of this section that the Fermi sea consists only of a single species of (spinless) electrons. The generalization to several channels needed in subsequent sections (in particular for discussing PS), is straightforward and will be introduced later as needed.

Although the concepts summarized in Secs. II B to II F below apply quite generically to a wide range of impurity models, for definiteness, we will illustrate them by referring to a particularly simple example, to be called the "local charge model" (LCM), which we define next.

A. Local charge model

The LCM describes a single spinless localized level, to be called dot level (alluding to a localized level in a quantum dot), interacting with a single Fermi sea of spinless electrons [see Fig. 1(a)]:

$$\hat{H}_{\rm LCM}(\hat{n}_d) = U\,\hat{n}_d\,\hat{c}^\dagger\hat{c} + \sum_\varepsilon \varepsilon\,\hat{c}^\dagger_\varepsilon\hat{c}_\varepsilon\,. \tag{2}$$

Here, $\hat{c}_\varepsilon$ and $\hat{d}$ are annihilation operators for Fermi sea states and the dot state, respectively, $\hat{n}_d = \hat{d}^\dagger\hat{d}$ counts the number of dot electrons, and $\hat{c} \equiv \hat{\psi}(0) \equiv \sum_\varepsilon \hat{c}_\varepsilon$ destroys a Fermi sea electron at the position of the dot. The interaction is taken to be repulsive, $U > 0$. There is no tunneling between dot and sea. Therefore the Hilbert space separates into two distinct sectors in which the local charge operator $\hat{n}_d$ has eigenvalues $n_d = 0$ and $n_d = 1$, respectively. The Hamiltonians describing the Fermi sea in the two distinct sectors are

$$\hat{H}_0 = \hat{H}_{\rm LCM}(n_d = 0) = \sum_\varepsilon \varepsilon\,\hat{c}^\dagger_\varepsilon\hat{c}_\varepsilon\,, \tag{3a}$$

$$\hat{H}_1(U) = \hat{H}_{\rm LCM}(n_d = 1) = \sum_\varepsilon \varepsilon\,\hat{c}^\dagger_\varepsilon\hat{c}_\varepsilon + U\hat{c}^\dagger\hat{c}\,. \tag{3b}$$

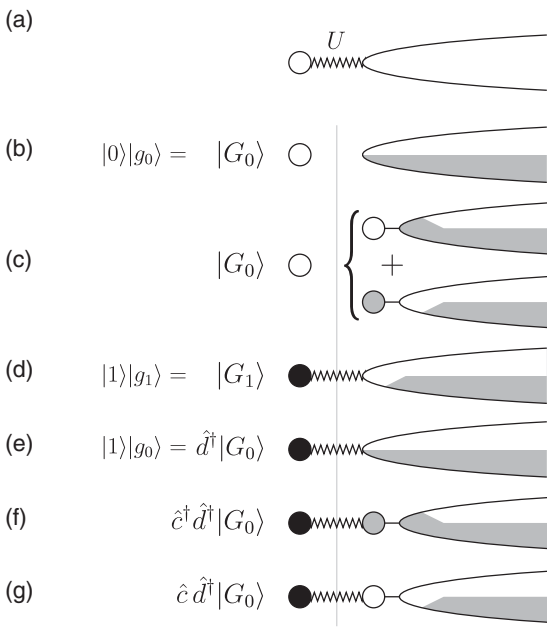

FIG. 1. (a) Cartoon of the Hamiltonian (2) for the LCM. (b)–(g) Cartoons of the occupation of the dot and a half-filled lead, for $U > 0$, for several states discussed in the text. (b) and (c) give two equivalent depictions of the ground state $|G_0\rangle$ of $\hat{H}_0$. (c) depicts the fact that $|g_0\rangle$ can be written as a superposition of the form $|0\rangle_{\rm c}|Q\rangle_{\rm rest} + |1\rangle_{\rm c}|Q-1\rangle_{\rm rest}$, indicating complementary occupations of the first site and the rest of a half-filled Wilson chain (defined in Sec. II F below). Here, $|0\rangle_{\rm c}$ (which obeys $\hat{c}|0\rangle_{\rm c} = 0$) and $|1\rangle_{\rm c} = \hat{c}^\dagger|0\rangle_{\rm c}$ describe the first site of the Wilson chain being empty or filled, respectively; the charge in the rest of the Wilson chain is correspondingly distributed in such a way that both components of the superposition have the same total charge, Q. (d) depicts the ground state $|G_1\rangle$ of $\hat{H}_1$, indicating that charge on the dot pushes charge in the lead away from the dot site. (e) shows the effect of applying $\hat{d}^\dagger$ to $|G_0\rangle$, the latter depicted according to (b). Similarly, (f) and (g) show the effect of applying $\hat{c}^\dagger\hat{d}^\dagger$ or $\hat{c}\hat{d}^\dagger$ to $|G_0\rangle$, the latter depicted according to (c). The displaced charge flowing inwards from infinity toward the dot as each of the states (e)–(g) evolves to the final ground state $|G_1\rangle$ of (d) is $\Delta_d < 0$, $\Delta_d - 1 < 0$ or $\Delta_d + 1 > 0$, respectively. Comparison of (f) and (g) with (e) shows average charge differences of $+1$ and -1, respectively, in accord with the Hopfield-type argument summarized by Eq. (15).

We will denote their respective ground states [illustrated in Figs. 1(b)–1(d), respectively] by

$$|G_0\rangle = |0\rangle|g_0\rangle\,, \quad |G_1\rangle = |1\rangle|g_1\rangle\,, \tag{4}$$

where $|0\rangle$ and $|1\rangle = \hat{d}^\dagger|0\rangle$ describe the dot state with charge 0 or 1, respectively, and $|g_0\rangle$ and $|g_1\rangle$ the corresponding Fermi sea ground states.

The LCM contains all ingredients needed for AO, hence we will repeatedly refer to it below as an explicit example of the general arguments to be presented. [Corresponding LCM passages will sometimes appear in square brackets, so as not to disrupt the general flow of the discussion.] Explicit numerical results for the LCM will be presented in Sec. III A below.

B. AO and the displaced charge

For the ensuing discussions, it will be useful to distinguish between two types of quenches, to be called type 1 and 2, which we now discuss in turn.

Type 1 quench. For a type 1 quench, some parameter of the Hamiltonian is changed abruptly (e.g., by a sudden change of gate voltage for one of the gates defining a quantum dot). Taking the LCM as an example, suppose that the value of the interaction in the LCM is changed suddenly from U to U' for a *fixed* local charge of $n_d = 1$. This corresponds to a type 1 quench with

$$\hat{H}_{\rm i} = \hat{H}_1(U)\,, \quad \hat{H}_{\rm f} = \hat{H}_1(U')\,, \tag{5a}$$

$$|G_{\rm i}\rangle = |1\rangle|g_{1,{\rm i}}\rangle\,, \quad |G_{\rm f}\rangle = |1\rangle|g_{1,{\rm f}}\rangle\,. \tag{5b}$$

The overlap of initial and final ground states,

$$|\langle G_{\rm i}|G_{\rm f}\rangle| = |\langle g_{1,{\rm i}}|g_{1,{\rm f}}\rangle| \sim N^{-\frac{1}{2}\Delta_{\rm AO}^2}\,, \tag{6}$$

will vanish in the thermodynamic limit due to AO, since the two Fermi sea states $|g_{1,{\rm i}}\rangle$ and $|g_{1,{\rm f}}\rangle$ feel scattering potentials of different strengths.

In his classic 1967 papers,[1,2] Anderson showed that for this type of situation the exponent $\Delta_{\rm AO}$ in Eq. (6) is equal to the change in scattering phase shifts at the Fermi surface divided by π, in reaction to the change in the strength of the scattering potential. (The correct expression for $\Delta_{\rm AO}$ first appeared in Ref. 2.) According to the Friedel sum rule,[22–25] the change in phase shifts divided by π, in turn, is equal to the *displaced charge* $\Delta_{\rm ch}$ (in units of e) that flows inward from infinity into a large but finite volume (say $V_{\rm large}$) surrounding the scattering site, in reaction to the change in scattering potential, so that $\Delta_{\rm AO} = \Delta_{\rm ch}$. To be explicit,

$$\Delta_{\rm ch} \equiv \langle G_{\rm f}|\hat{n}_{\rm tot}|G_{\rm f}\rangle - \langle G_{\rm i}|\hat{n}_{\rm tot}|G_{\rm i}\rangle\,, \tag{7}$$

where $\hat{n}_{\rm tot} \equiv \hat{n}_{\rm sea} + n_{\rm dot}$ counts the *total* number of electrons within $V_{\rm large}$, with $\hat{n}_{\rm sea}$ counting the Fermi sea electrons and $\hat{n}_{\rm dot}$ counting the electrons on the dot. [For the LCM, $\hat{n}_{\rm dot} = \hat{n}_d$.]

The relative sign between $\Delta_{\rm AO}$ and $\Delta_{\rm ch}$ (+ not −) is a matter of convention, which does not affect the orthogonality exponent $\Delta_{\rm AO}^2$. Our convention,[21] which agrees with standard usage,[26] is such that $\Delta_{\rm AO} > 0$ (or <0) if the change in local potential induces electrons to flow inward toward (outward away from) the scattering site.

For the LCM quench of Eq. (5) above, the initial and final states have the same dot charge, $n_d = 1$, hence the displaced charge reduces to $\Delta_{\rm ch} \equiv \langle g_{1,{\rm f}}|\hat{n}_{\rm sea}|g_{1,{\rm f}}\rangle - \langle g_{1,{\rm i}}|\hat{n}_{\rm sea}|g_{1,{\rm i}}\rangle$. However, such a simplification will not occur for more complex impurity models involving tunnelling between dot and lead [of the form $(\hat{d}^\dagger\hat{c} + \hat{c}^\dagger\hat{d})$], so that the local charge is not conserved. Examples are the interacting resonant level model [see Eq. (40) below], or the single-impurity Anderson model [see Eq. (51) below].

For such a model, consider a type 1 quench from $\hat{H}_{\rm i}$ to $\hat{H}_{\rm f}$, implemented by a sudden change in one or several model parameters, in analogy to Eq. (5a). Although the corresponding ground states $|G_{\rm i}\rangle$ and $|G_{\rm f}\rangle$ will no longer have the simple factorized form of Eq. (5b), they will still exhibit AO as in Eq. (1). Moreover, the decay exponent is still equal to the displaced charge, $\Delta_{\rm AO} = \Delta_{\rm ch}$, given by Eq. (7). (For a NRG verification of this fact, see Ref. 21.)

Type 2 quench. For a type 2 quench, all model parameters are kept constant, but the system is switched suddenly between two dynamically disconnected sectors of Hilbert space characterized by different conserved quantum numbers. Taking again the LCM of Eq. (2) as an example, suppose that the local charge is suddenly changed, say from $n_d = 0$ to 1, while all model parameters are kept constant. This corresponds to a type 2 quench with

$$\hat{H}_{\rm i} = \hat{H}_0, \qquad \hat{H}_{\rm f} = \hat{H}_1\,, \tag{8a}$$

$$|G_{\rm i}\rangle = |0\rangle|g_0\rangle, \quad |G_{\rm f}\rangle = |1\rangle|g_1\rangle. \tag{8b}$$

A physical example of such a quench would be core level x-ray photoemission spectroscopy (XPS), where an incident x-ray photon is absorbed by an atom in a crystal, accompanied by the ejection of a core electron from the material.[27] This amounts to the sudden creation of a core hole, which subsequently interacts with the Fermi sea of mobile conduction electrons (but does not hybridize with them). Thus, in this example, $\hat{n}_d$ would represent the hole number operator $\hat{n}_h = \hat{h}^\dagger\hat{h}$.

More generally, a type 2 quench presupposes a Hamiltonian $\hat{H}(\hat{n}_x)$ that depends on a conserved charge, say $\hat{n}_x$ [such as $\hat{n}_d$ for the LCM], with eigenvalues n_x [such as $n_d = 0$ or 1]. The Hilbert space can then be decomposed into distinct, dynamically disconnected sectors, labeled by n_x and governed by effective Hamiltonians $\hat{H}(n_x)$, whose ground states have the form $|G(n_x)\rangle = |n_x\rangle|g(n_x)\rangle$. A type 2 quench is induced by an operator, say $\hat{X}^\dagger$ [such as $\hat{d}^\dagger$ for the LCM], whose action changes the conserved charge, thereby connecting two distinct sectors, say $\langle n_x'|\hat{X}^\dagger|n_x\rangle = 1$, with $n_x' \neq n_x$. For such a quench, we make the identifications

$$\hat{H}_{\rm i} = \hat{H}(n_x), \quad \hat{H}_{\rm f} = \hat{H}(n_x')\,, \tag{9a}$$

$$|G_{\rm i}\rangle = |n_x\rangle|g(n_x)\rangle, \quad |G_{\rm f}\rangle = |n_x'\rangle|g(n_x')\rangle. \tag{9b}$$

The overlap $\langle G_{\rm i}|G_{\rm f}\rangle = 0$ vanishes trivially, because $\langle n_x|n_x'\rangle = 0$. However, define

$$|\psi_{\rm i}\rangle \equiv \hat{X}^\dagger|G_{\rm i}\rangle \tag{10}$$

to be the "initial postquench state" obtained by the action of the charge switching operator $\hat{X}^\dagger$ on the initial ground state. [Fig. 1(e) illustrates this state for the LCM with $\hat{X}^\dagger = \hat{d}^\dagger$.] Then the overlap

$$\mathcal{O}_X \equiv |\langle\psi_{\rm i}|G_{\rm f}\rangle| = |\langle g(n_x)|g(n_x')\rangle| \sim N^{-\frac{1}{2}\Delta_X^2} \tag{11}$$

again shows AO, since it is equal to the overlap of two Fermi sea ground states corresponding to different local charges. The corresponding exponent in Eq. (11) can again be related to a displaced charge, $\Delta_X = \Delta_X^{\rm ch}$, but now the latter should compare the total charge within $V_{\rm large}$ described by the states $|G_{\rm f}\rangle$ and $|\psi_{\rm i}\rangle$:

$$\Delta_X^{\rm ch} \equiv \langle G_{\rm f}|\hat{n}_{\rm tot}|G_{\rm f}\rangle - \langle\psi_{\rm i}|\hat{n}_{\rm tot}|\psi_{\rm i}\rangle\,. \tag{12}$$

$\Delta_X^{\rm ch}$ can be interpreted as the charge (in units of e) that flows into $V_{\rm large}$ during the post-quench time evolution from $|\psi_{\rm i}\rangle$ to $|G_{\rm f}\rangle$ subsequent to the action of $\hat{X}^\dagger$. To simplify notation, we will often omit the superscript "ch" distinguishing the displaced charge $\Delta_X^{\rm ch}$ from the AO exponent Δ_X, since the two are equal in any case.

Composite type 2 quench. Let us now consider a more complicated version of a type 2 quench, induced by a composite operator of the form $\hat{Y}^\dagger = \hat{C}^\dagger \hat{X}^\dagger$. Here, $\hat{X}^\dagger$ switches between disconnected sectors of Hilbert space as above, while $\hat{C}^\dagger$ does not; instead, $\hat{C}^\dagger$ is assumed to be a *local* operator which acts on the dot or in the Fermi sea at the location of the dot, but commutes with $\hat{n}_x$. For the LCM, an example would be $\hat{C}^\dagger = \hat{c}^\dagger$, so that $\hat{Y}^\dagger$ creates two electrons, one on the dot, one in the Fermi sea at the site of the dot.

A physical realization hereof is furnished by the edge-ray edge effect occurring in x-ray absorption spectroscopy (XAS), where an incident x-ray photon is absorbed by an atom in a crystal, accompanied by the creation of a core hole ($\hat{X}^\dagger = \hat{h}^\dagger$) and the transfer of a core electron into the conduction band of the metal ($\hat{C}^\dagger = \hat{c}^\dagger$).[27] Another example is the Kondo exciton discussed in Refs. 15 and 16, where the absorption of a photon by a quantum dot is accompanied by the creation of an electron-hole pair on the dot, described by $\hat{C}^\dagger = \hat{e}^\dagger$ and $\hat{X}^\dagger = \hat{h}^\dagger$, respectively. In this example, the hole number $\hat{n}_h = \hat{h}^\dagger \hat{h}$ is conserved, but the dot electron number $\hat{n}_e = \hat{e}^\dagger \hat{e}$ is not, since the Hamiltonian contains dot-lead hybridization terms of the form $(\hat{e}^\dagger \hat{c} + \hat{c}^\dagger \hat{e})$ (see Refs. 15 and 16 for details).

For a composite type 2 quench, the initial and final Hamiltonians and ground states are defined as in Eqs. (5), but the postquench initial state is given by

$$|\psi_{\rm i}'\rangle \equiv \hat{Y}^\dagger |G_{\rm i}\rangle = \hat{C}^\dagger |\psi_{\rm i}\rangle \,, \tag{13}$$

with $|\psi_{\rm i}''\rangle \equiv \mathcal{N}|\psi_{\rm i}'\rangle$ the normalized postquench initial state and $\mathcal{N}$ a normalization constant. The overlap of $|\psi_{\rm i}'\rangle$ with the final ground state $|G_{\rm f}'\rangle$ to which it evolves in the long-time limit has the form

$$\mathcal{O}_Y \equiv |\langle \psi_{\rm i}'|G_{\rm f}'\rangle| = |\langle g(n_x)|\hat{C}|g'(n_x')\rangle| \sim N^{-\frac{1}{2}\Delta_Y^2} \,. \tag{14}$$

The exponent Δ_Y arising here is related to Δ_X and can be found using the following argument, due to Hopfield.[5] Due to the action of $\hat{C}^\dagger$, the states $|\psi_{\rm i}'\rangle$ and $|\psi_{\rm i}\rangle$ describe different amounts of initial postquench charge within the volume $V_{\rm large}$. We will denote the difference by

$$\Delta_C \equiv \langle \psi_{\rm i}''|\hat{n}_{\rm tot}|\psi_{\rm i}''\rangle - \langle \psi_{\rm i}|\hat{n}_{\rm tot}|\psi_{\rm i}\rangle \,. \tag{15}$$

For example, if $\hat{C}^\dagger$ is a local electron creation or annihilation operator, then $\Delta_C = 1$ or -1, respectively [as illustrated in Figs. 1(f) and 1(g)]. However, since an initial charge surplus or deficit at the scattering site is compensated, in the long-time limit, by charges flowing to or from infinity, the ground states $|G_{\rm f}'\rangle$ and $|G_{\rm f}\rangle$ toward which $|\psi_{\rm i}'\rangle$ and $|\psi_{\rm i}\rangle$ evolve, respectively, will differ only by one Fermi sea electron at infinity, and hence for practical purposes describe the same local physics. In particular, the charge within $V_{\rm large}$ is the same for both, $\langle G_{\rm f}'|\hat{n}_{\rm tot}|G_{\rm f}'\rangle = \langle G_{\rm f}|\hat{n}_{\rm tot}|G_{\rm f}\rangle$. Therefore the *total* displaced charge associated with the action of $\hat{Y}^\dagger$ is

$$\Delta_Y \equiv \langle G_{\rm f}'|\hat{n}_{\rm tot}|G_{\rm f}'\rangle - \langle \psi_{\rm i}''|\hat{n}_{\rm tot}|\psi_{\rm i}''\rangle = \Delta_X - \Delta_C, \tag{16}$$

where the second equality follows from Eqs. (12) and (15). The exponent governing the AO decay in Eq. (14) is thus given by Eq. (16). Since Δ_C is a trivially known integer, knowledge of Δ_X for a type 2 quench suffices to determine the AO exponents Δ_Y for an entire family of related composite quenches.

To conclude this section, we note that a type 1 quench can always be formulated as a type 2 quench, by introducing an auxiliary conserved degree of freedom (say $\hat{n}_h$), whose only purpose is to divide the Hilbert space into two sectors (labelled by $n_h = 0$ or 1), within which some parameters of the Hamiltonian take two different values. For example, if the quench involves changing U to U', this can be modelled by replacing U by $U + \hat{n}_h(U' - U)$ in the Hamiltonian. For an example, see Sec. III C.

C. AO and postquench time evolution

After a sudden change in the local Hamiltonian, AO also affects the long-time limit of the subsequent time evolution, and hence the low-frequency behavior of corresponding spectral functions. A prominent example is optical absorption,[3–6,14–16] for which AO leaves its imprint in the shape of the absorption spectrum, by reducing the probability for absorption. This is familiar from the x-ray edge problem.[4] In particular, in the limit of absorption frequency ω very close to (but above) the threshold for absorption, the zero-temperature absorption spectrum has a power-law form, with an exponent that is influenced by AO. Recent demonstrations of this fact can be found in studies, both theoretical[14,15] and experimental,[16] of exciton creation in quantum dots via optical absorption, whereby an electron is excited from a valence-band level to a conduction band level.

In this section, we will analyze the role of AO for the time evolution after a type 2 quench of the form (8). We consider the following generic situation. For $t < 0$, a system is in the ground state $|G_{\rm i}\rangle$ of the initial Hamiltonian $\hat{H}_{\rm i}$ (with ground-state energy $E_{\rm i}$), describing a Fermi sea under the influence of a local scattering potential. At $t = 0$, a sudden change in the local potential occurs, described by the action the local operator $\hat{X}^\dagger$. It switches sector n_x to n_x', yielding the post-quench initial state $|\psi_{\rm i}\rangle = \hat{X}^\dagger|G_{\rm i}\rangle$ at time $t = 0^+$, and switches the Hamiltonian from $\hat{H}_{\rm i}$ to $\hat{H}_{\rm f}$.

The subsequent dynamics can be characterized by the correlator

$$\mathcal{G}_X(t) \equiv -ie^{i\omega_0 t}\theta(t)\langle G_{\rm i}|\hat{X}(t)\hat{X}^\dagger|G_{\rm i}\rangle \,, \tag{17}$$

where $\hat{X}(t) = e^{i\hat{H}_{\rm i}t}\hat{X}e^{-i\hat{H}_{\rm f}t}$, reflecting the fact that $\hat{X}$ switches $\hat{H}_{\rm f}$ to $\hat{H}_{\rm i}$. The phase factor $e^{i\omega_0 t}$ is included for later convenience, with ω_0 to be specified below [after Eq. (26)].

Since the Fermi sea adjusts in reaction to the sudden change in local potential at $t = 0$, AO builds up and the overlap function $\mathcal{G}_X(t)$ decreases with time. It is known since 1969 that in the long-time limit, it decays in power-law fashion as[3,5]

$$\mathcal{G}_X(t) \sim t^{-\Delta_X^2} \,, \tag{18}$$

where Δ_X is the exponent governing the AO decay of $\mathcal{O}_X$ in Eq. (11). This can be understood heuristically by expanding Eq. (17) as

$$ie^{-i(E_{\rm i}+\omega_0)t}\mathcal{G}_X(t) = \theta(t)\langle\psi_{\rm i}|e^{-i\hat{H}_{\rm f}t}|\psi_{\rm i}\rangle \tag{19a}$$

$$= \theta(t)\langle\psi_{\rm i}|\psi_{\rm i}(t)\rangle \tag{19b}$$

$$= \theta(t)\sum_n e^{-iE_n t}|\langle\psi_{\rm i}|n\rangle|^2 \,, \tag{19c}$$

where $|\psi_{\rm i}(t)\rangle = e^{-i\hat{H}_{\rm f}t}|\psi_{\rm i}\rangle$ describes the time-evolution for $t > 0$, and $|n\rangle$ and E_n represent a complete set of eigenstates and eigenenergies of $\hat{H}_{\rm f}$. In the long-time limit, Eq. (19c) will

be dominated by the ground state $|G_f\rangle$ of $\hat{H}_f$ (with eigenenergy E_f), yielding a contribution $|\langle\psi_i|G_f\rangle|^2$ that scales as $N^{-\Delta_X^2}$ [by Eq. (11)]. Now, as time increases, the effect of the local change in scattering potential is felt at increasing length scales $L(t) \sim v_f t$, with v_f the Fermi velocity; regarding $|G_f\rangle$ as the lowest eigenstate of $\hat{H}_f$ in a box of size $N \sim L(t)$, the AO of $|\langle\psi_i|G_f\rangle|^2 \sim L(t)^{-\Delta_X^2}$ implies Eq. (18).

For a composite type 2 quench induced by $\hat{Y}^\dagger = \hat{C}^\dagger \hat{X}^\dagger$, we can conclude by analogous arguments that the correlation function

$$\mathcal{G}_Y(t) \equiv -ie^{i\omega_0 t}\theta(t)\langle G_i|\hat{Y}(t)\hat{Y}^\dagger|G_i\rangle \,, \tag{20}$$

behaves in the long-time limit as a power-law

$$\mathcal{G}_Y(t) \sim t^{-\Delta_Y^2} \,, \tag{21}$$

where Δ_Y is the displaced charge of Eq. (16).

D. Effects of AO on nonquench dynamics

Up to now, we assumed that operators such as $\hat{Y}$ transfer the system between *decoupled* sectors of the Hilbert space. However, the value of Δ_Y^2 obtained in this decoupled case is also important in determining the behavior of the system if one modifies the Hamiltonian by introducing a local perturbation of the form

$$\hat{H}_Y = \gamma_Y \hat{Y} + \text{H.c.}, \tag{22}$$

which couples the two dynamical sectors, where γ_Y (assumed to have units of energy) is small with respect to the other energy scales in the problem. For example, in the LCM, Eq. (2), $\hat{Y}$ could be a tunneling term, $\hat{Y} = \hat{c}^\dagger \hat{d}$, as we discuss in much more detail in Sec. III. By Eq. (21), the scaling dimension of $\hat{H}_Y$ around the "disconnected sectors fixed point" $\gamma_Y = 0$ is $\eta_Y = \Delta_Y^2/2$. This means that to lowest order in γ_Y, the RG flow of γ_Y upon reducing a high-energy cutoff is governed by the following RG equation:[28]

$$D_{\text{RG}} \frac{d(\gamma_Y/D_{\text{RG}})}{dD_{\text{RG}}} = (\eta_Y - 1)\frac{\gamma_Y}{D_{\text{RG}}} \,, \tag{23}$$

where D_{RG} is the running cutoff, which decreases along the flow. Its initial value is the "bare" cutoff of the unrenormalized system, to be denoted by D. Thus γ_Y is relevant, marginal or irrelevant under renormalization around this fixed point if $\eta_Y < 1, = 1,$ or > 1, respectively.[28] If γ_Y is irrelevant, its effect is perturbative and to leading order, the system behaves as if $\gamma_Y = 0$. If γ_Y is relevant, it grows until γ_Y/D_{RG} becomes of order 1 (assuming γ_Y has units of energy), and Eq. (23) loses its validity. This happens at an energy (cutoff) scale of

$$D^* = D\left(\frac{\gamma_Y}{D}\right)^{1/(1-\eta_Y)} \,. \tag{24}$$

Hence, at energies (temperature, frequency, etc.) above D^* the system is in the vicinity of the $\gamma_Y = 0$ fixed point, and γ_Y can be treated perturbatively. At energies lower than D^*, the behavior will, in general, be governed by a new, strong-γ_Y fixed point, where the previously separate sectors become strongly coupled. The details would then depend on the specific system. In addition, observables (expectation values and correlation functions) will show scaling behavior as a function of, e.g., temperature and frequency, when energies are measured in units of D^* and are small with respect to the cutoff D.

For future reference, we also introduce the correlator

$$\mathcal{G}_C^{\text{eq}}(t) \equiv -i\theta(t)\langle G|e^{i\hat{H}t}\hat{C}e^{-i\hat{H}t}\hat{C}^\dagger|G\rangle \sim it^{-2\eta_C^{\text{eq}}} \tag{25}$$

of an operator $\hat{C}^\dagger$ that does not switch between dynamically disconnected sectors, i.e., that commutes with $\hat{n}_x$ [examples of such operators are given in the discussion before Eq. (13) above]. Similarly, in the presence of the $\hat{Y}$ term in Eq. (22), $\hat{n}_x$ is not conserved, and the operators $\hat{X}$ or $\hat{Y}$ themselves no longer switch between disconnected sectors. Then Eq. (25) is a standard *equilibrium* correlator, with $\hat{H}_i = \hat{H}_f$, in contrast to the *quench* correlator $\mathcal{G}_X(t)$ of Eq. (25), where $\hat{H}_i \neq \hat{H}_f$. In the rest of this section, we return to the disconnected case, where terms such as $\hat{Y}$ in Eq. (22) are absent ($\gamma_Y = 0$).

E. AO and spectral functions

Next, we consider the spectral function corresponding to $\mathcal{G}_X(t)$,

$$\mathcal{A}_X(\omega) \equiv -\frac{1}{\pi}\Im\left[\int_0^\infty dt e^{i(\omega+i0^+)t}\mathcal{G}_X(t)\right] \tag{26a}$$

$$= \sum_n |\langle n|\hat{X}^\dagger|G_i\rangle|^2 \delta(\omega - E_n + E_i + \omega_0) \,. \tag{26b}$$

It evidently has the form of a golden-rule transition rate for $\hat{X}^\dagger$-induced transitions with excitation energy $\omega + \omega_0$ and is nonzero only for ω above the threshold frequency $\omega_{\text{th}} = (E_f - E_i) - \omega_0$. For simplicity, we will here and henceforth set $\omega_{\text{th}} = 0$ by choosing $\omega_0 = E_f - E_i$. Note the sum rule $\int d\omega \mathcal{A}(\omega) = \langle G_i|\hat{X}\hat{X}^\dagger|G_i\rangle$, which can be used as consistency check for numerical calculations.

Equation (18) implies that in the limit $\omega \to \omega_{\text{th}} = 0$, the spectral function behaves as

$$\mathcal{A}_X(\omega) \sim \omega^{-1+2\eta_X} \,, \quad \eta_X = \tfrac{1}{2}\Delta_X^2 \,. \tag{27}$$

Now consider the spectral function $\mathcal{A}_Y(\omega)$ involving the composite type 2 quench operator $\hat{Y}^\dagger = \hat{C}^\dagger \hat{X}^\dagger$,

$$\mathcal{A}_Y(\omega) \equiv -\frac{1}{\pi}\Im\left[\int_0^\infty dt e^{i(\omega+i0^+)t}\mathcal{G}_Y(t)\right] \tag{28a}$$

$$= \sum_n |\langle n|\hat{Y}^\dagger|G_i\rangle|^2 \delta(\omega - E_n + E_i + \omega_0) \,. \tag{28b}$$

Equations (21) and (16) immediately lead to the prediction

$$\mathcal{A}_Y(\omega) \sim \omega^{-1+2\eta_Y} \,, \quad \eta_Y = \tfrac{1}{2}(\Delta_X - \Delta_C)^2 \,, \tag{29}$$

to be called the *generalized Hopfield rule*, since the essence of the argument by which we have obtained it was first formulated by Hopfield.[5]

A physical situation for which Eq. (29) is relevant is the edge-ray edge effect occurring in x-ray absorption spectroscopy (XAS). There we have $\hat{Y}^\dagger = \hat{c}^\dagger \hat{h}^\dagger$ (as explained above), and $\Delta_C = 1$. Thus Eq. (29) yields

$$\mathcal{A}_{hc}(\omega) \sim \omega^{-1+(\Delta_h-1)^2} = \omega^{-2\Delta_h+\Delta_h^2} \tag{30}$$

reproducing a well-established result for the x-ray edge absorption spectrum [Ref. 5, p. 48; Ref. 6, Eq. (66)]. In the literature, $-2\Delta_h$ is often called the "Mahan contribution" to the exponent, and Δ_h^2 the AO contribution. Since $\Delta_h \leqslant 1$, one

has $2\Delta_h > \Delta_h^2$, i.e., "Mahan wins," and $\mathcal{A}_{hc}(\omega)$ diverges at small frequencies. For present purposes, though, it is perhaps somewhat more enlightening to adopt Hopfield's point of view, stated in Eq. (29), according to which both terms, $-2\Delta_h$ and Δ_h^2 arise from the AO exponent $(\Delta_h - 1)^2$.

Equations (11), (27), and (29) will play a central role in this work. Their message is that the near-threshold behavior of spectral functions of the type defined in Eq. (26) is governed by an AO exponent that can be extracted from the overlap $\langle\psi_i|G_f\rangle$ between the initial postquench state $|\psi_i\rangle$ and the ground state $|G_f\rangle$ to which it evolves in the long-time limit.

To conclude this section, we remark that the above analysis generalizes straightforwardly to models involving several species or channels of electrons, say with index μ, provided that the channel index is a conserved quantum number (i.e., no tunneling between channels occurs).[21] Then the initial and final ground states will be products of the ground states for each separate channel, so that Eq. (1) generalizes to

$$|\langle G_i|G_f\rangle| \sim \prod_\mu N_\mu^{-\frac{1}{2}\Delta^2_{\mathrm{AO},\mu}} . \tag{31}$$

All power laws discussed above that involve Δ^2_{AO} (or quantities derived therefrom) in the exponent can be similarly generalized by including appropriate products over channels.

F. AO exponents and NRG

Results of the above type have been established analytically, in the pioneering papers from 1969, Refs. 3–6, only for the simple yet paradigmatic case of the x-ray edge effect. Nevertheless, relations such as Eqs. (18), (21), and (29) can be expected to hold for a larger class of models, as long as the setting outlined above applies. Indeed, they have been fruitfully evoked in numerous works in the past, including the famous Anderson-Yuval treatment of the anisotropic Kondo model[29] and recent NRG studies thereof,[30] works on electron tunneling in metals,[8] studies of the auxiliary spectral functions for pseudofermions and slave bosons for the $U = \infty$ single-impurity Anderson model,[31] an analysis of a quantum phase transition involving Ising-coupled Kondo impurities,[32,33] and recent studies of the Kondo exciton,[14–16] to name but a few. The purpose of the present work is to systematically explore the validity of the connections between the AO overlap of Eq. (11) and the frequency-domain correlators of Eqs. (27) and (29), for a series of models of increasing complexity. We shall do so numerically using NRG, since for most of these models an analytical treatment along the lines of Refs. 3 and 6 would be exceedingly tedious, if not impossible. However, the requisite numerical tools are available within NRG,[31,34] and have become very accurate quantitatively due to recent methodological refinements.[15,35,36]

NRG, developed in the context of quantum impurity models, offers a very direct way of evaluating the overlap, since it allows both ground states $|G_i\rangle$ and $|G_f\rangle$ to be calculated explicitly. Models treatable by NRG have the generic form $\hat{H} = \hat{H}_B + \hat{H}_d$. Here,

$$\hat{H}_B = \sum_{\mu=1}^{n_c} \sum_\varepsilon \varepsilon\, \hat{c}^\dagger_{\varepsilon\mu} \hat{c}_{\varepsilon\mu} \tag{32}$$

describes a free Fermi sea involving n_c channels of fermions, with constant density of states ρ per channel and half-bandwidth $D = 1/(2\rho)$. (When presenting numerical results, energies will be measured in units of half-bandwidth by setting $D = 1$.) $\hat{H}_d$, which may involve interactions, describes local degrees of freedom and their coupling to the Fermi sea.

Wilson discretized the spectrum of $\hat{H}_0$ on a logarithmic grid of energies $\pm D\Lambda^{-k}$ (with $\Lambda > 1$, $k = 0,1,2,\ldots$), thereby obtaining exponentially high resolution of low-energy excitations. He then mapped the impurity model onto a semi-infinite "Wilson tight-binding chain" of sites $k = 0$ to ∞, with the impurity degrees of freedom coupled only to site 0. To this end, he made a basis transformation from the set of Fermi sea operators $\{\hat{c}_{\varepsilon\mu}\}$ to a new set $\{\hat{f}_{k\mu}\}$, with $\hat{f}_{0\mu} \propto \hat{c}_\mu \equiv \psi_\mu(0) \equiv \sum_\varepsilon \hat{c}_{\varepsilon\mu}$, chosen such that they bring $\hat{H}_0$ into the tridiagonal form

$$\hat{H}_B \simeq \sum_{\mu=1}^{n_c} \sum_{k=1}^{\infty} t_k (\hat{f}^\dagger_{k\mu} \hat{f}_{k-1,\mu} + \mathrm{H.c.}) , \tag{33}$$

with hopping matrix elements $t_k \propto D\Lambda^{-k/2}$ that decrease exponentially with site index k along the chain. Because of this separation of energy scales, the Hamiltonian can be diagonalized iteratively by solving a Wilson chain of length k [restricting the sum in Eq. (33) to the first k terms] and increasing k one site at a time. The number of kept states at each iteration will be denoted by N_k.

For a Wilson chain of length k, the effective level spacing of its lowest-lying energy levels is set by the smallest hopping matrix element of the chain, namely $\Lambda^{-k/2}$; such a Wilson chain thus represents a real space system of volume $V_{\mathrm{large}} \sim \Lambda^{k/2}$. Thus the overlap between the two ground states of a Wilson chain of length k can be expressed as[21]

$$|{}_k\langle G_i|G_f\rangle_k| \sim \Lambda^{-\frac{k}{4}\Delta^2_{\mathrm{AO}}} \equiv e^{-\alpha k} , \tag{34}$$

where $\alpha \equiv (\log\Lambda/4)\Delta^2_{\mathrm{AO}}$. Explicit calculations show[21] that an exponential decay of the form Eq. (34) applies for the overlap between any two states $|E_i\rangle_k$ and $|E_f\rangle_k$ representing low-lying excitations with respect to $|G_i\rangle_k$ and $|G_f\rangle_k$ at iteration k, respectively. More technically, ${}_k\langle E_i|E_f\rangle_k \sim e^{-\alpha k}$ holds whenever $|E_i\rangle_k$ and $|E_f\rangle_k$ represent NRG eigenstates with matching quantum numbers from the kth NRG shell for $\hat{H}_i$ and $\hat{H}_f$, respectively, and their overlap is calculated for increasing k. For multichain models, we note that channel-specific exponents such as $\Delta_{\mathrm{AO},\mu}$ [see Eq. (31)] can be calculated, if needed, by considering Wilson chains with channel-dependent lengths.[21]

Within the framework of NRG, a consistency check is available for the value of Δ_{AO} extracted from Eq. (34): Δ_{AO} should be equal to the displaced charge Δ_{ch} of Eq. (7), which can also be calculated directly from NRG by calculating the expectation value of $\hat{n}_{\mathrm{tot}}$ for $|G_i\rangle$ and $|G_f\rangle$ individually.[21] This check was successfully performed, for example, in Refs. 14 and 15, within the context of the single impurity Anderson model; for a recent systematic study, see Ref. 21. We have also performed this check in the present work wherever it was feasible.

Within NRG, it is also possible to directly calculate spectral functions such as $\mathcal{A}_X(\omega)$ of Eq. (26). To this end, one uses two separate NRG runs to calculate the ground state $|G_i\rangle$ of $\hat{H}_i$

and an approximate but complete set of eigenstates $|n\rangle$ of $\hat{H}_{\rm f}$.[35,36] The Lehmann sum in Eq. (26) can then be evaluated explicitly,[37,38] while representing the δ functions occurring therein using a logarithm-Gaussian broadening scheme. To this end, we follow the approach of Ref. 38, which involves a broadening parameter σ. (The specific choice of NRG parameters Λ, N_k, and σ used for spectral data shown below will be specified in the legends of the corresponding figures.) That this approach is capable of yielding spectral functions whose asymptotic behaviour shows power-law behavior characteristic of AO has been demonstrated recently in the context of the Kondo exciton problem.[14–16] In the examples to be discussed below, we will compare the power-law exponents extracted from the asymptotic behavior of such spectral functions to the values expected from AO, thus checking relations such as Eq. (27) for $\mathcal{A}_X(\omega)$ and Eq. (29) for $\mathcal{A}_Y(\omega)$.

III. INTERACTING RESONANT LEVEL MODEL

In this section, we consider the effect of AO on dynamical quantities in the context of the spinless interacting resonant level model (IRLM).[13,39] (The effects of AO for some static properties of this model were studied in Ref. 30.) The purpose of this exercise is to illustrate several effects that will be found to arise also for more complex models considered in subsequent sections. The IRLM involves a single localized level, to be called dot level (alluding to localized levels in a quantum dot), interacting with and tunnel coupled to a single Fermi sea. We consider first the case without tunneling, in which case the IRLM reduces to the LCM introduced in Sec. II above, where adding an electron to the dot at time $t = 0$ constitutes a type 2 quench. This leads to AO between the initial and final ground states, and corresponding nontrivial AO power laws, $\omega^{-1+2\eta}$, in spectral functions. We then turn on tunneling, which connects the sectors of Hilbert space for which the dot is empty or filled, and hence counteracts AO. Correspondingly, the power-laws get modified at frequencies smaller than the renormalized level width, $\omega \lesssim \Gamma_{\rm ren}$, where the AO behaviour is replaced by simple Fermi liquid behavior; the effects of AO do survive, however, in a regime of intermediate frequencies, $\Gamma_{\rm ren} < \omega < D$. Finally, we consider quenches of the position of the dot level, in which case AO reemerges.

A. Without tunneling: LCM

In this section, we present numerical results for the IRLM without tunnelling, corresponding to the local charge model of Eq. (2), depicted in Fig. 1(a). We consider the type 2 quench of Eq. (5), with $\hat{X}^\dagger = \hat{d}^\dagger$. The initial and final ground states $|G_{\rm i}\rangle$ and $|G_{\rm f}\rangle$ are illustrated in Figs. 1(b)–1(d), respectively, and the postquench initial state $|\psi_{\rm i}\rangle = \hat{d}^\dagger|G_{\rm i}\rangle$ in Fig. 1(e). With these choices the overlap $|\langle\psi_{\rm i}|G_{\rm f}\rangle|$ of Eq. (11) becomes

$$\mathcal{O}_d \equiv |\langle G_0|\hat{d}|G_1\rangle| = |\langle g_0|g_1\rangle| \sim N^{-\frac{1}{2}\Delta_d^2} . \qquad (35)$$

The corresponding displaced charge obtained from Eq. (12) is

$$\Delta_d^{\rm ch} = \langle g_1|\hat{n}_{\rm sea}|g_1\rangle - \langle g_0|\hat{n}_{\rm sea}|g_0\rangle , \qquad (36)$$

since $|G_{\rm f}\rangle$ and $|\psi_{\rm i}\rangle$ describe the same dot charge, $n_d = 1$.

We used NRG to calculate the overlap $\mathcal{O}_d$ of Eq. (35) and extract the exponent Δ_d from its exponential decay with Wilson chain length [see Eq. (34)], for several values of U. As a consistency check, we also calculated the displaced charge $\Delta_d^{\rm ch}$ [see Eq. (36)]. As shown in Fig. 2(a), the results for Δ_d (crosses) and $\Delta_d^{\rm ch}$ (pluses) agree very well. The displaced charge $\Delta_d^{\rm ch}$ is <0, since the repulsive interaction pushes charge away from the local site. Its magnitude $|\Delta_d^{\rm ch}|$ depends on the interaction strength: as U is increased from 0 to ∞, the displaced charge goes from 0 to $-\frac{1}{2}$, reflecting the complete depletion of the initially half-filled Wilson chain site directly adjacent to the dot site [compare Figs. 1(b) and 1(d)]. Figure 2(a) shows that the numerical results for Δ_d and $\Delta_d^{\rm ch}$ (symbols) also agree with the analytical result (solid line) obtained for the phase shift obtained from elementary scattering theory [see, e.g., Ref. 13, Eq. (25.29)],

$$\Delta_d = -\frac{1}{\pi}\tan^{-1}(\pi\rho U) , \qquad (37)$$

with ρ the density of states in the Fermi sea (cf. Sec. II F).

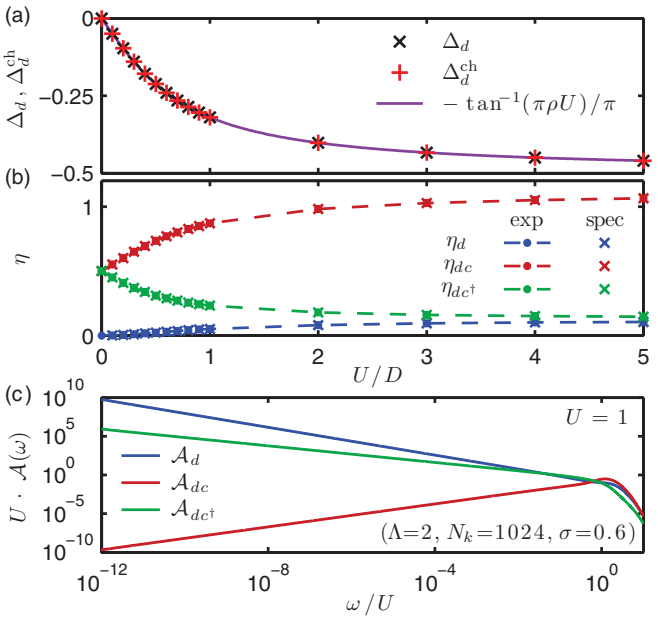

FIG. 2. (Color online) Numerical results for the LCM of Eq. (2), for the type 2 quench of Eq. (8), whose initial, final, and postquench initial states $|G_{\rm i}\rangle$, $|G_{\rm f}\rangle$, and $|\psi_{\rm i}\rangle$ are depicted in Figs. 1(b)–1(d) and 1(e)–1(g), respectively. (a) Comparison of the decay exponent Δ_d obtained from Eq. (35) (crosses) with the displaced charge $\Delta_d^{\rm ch}$ from Eq. (36) (pluses) for a number of different values of U. The two values agree very well (they differ by less than 0.1%), also with the analytic prediction Eq. (37) (solid line). As expected, $\Delta_d \to -1/2$ for $U \to \infty$. (b) Comparison of two ways of determining the AO exponents η that govern the low-energy asymptotic behaviour $\mathcal{A} \sim \omega^{-1+2\eta}$ of the spectral functions of Eqs. (39), related to Figs. 1(e)–1(g): exponents obtained by fitting a power law to the corresponding spectra [shown in (c)] are shown as crosses (marked "spec" for "spectra"); the corresponding exponents expected from Eq. (39), using the results of (a) for Δ_d, are shown as dots (marked "exp" for "expected"). We find a maximal deviation of less than 1%. Here and in all similar figures below, the dashed lines are only guides to the eye. (c) Asymptotic low-frequency dependence of the spectra Eqs. (39), for $U = 1$, on a double logarithmic plot, allowing the corresponding exponents η to be extracted.

To study the influence of AO on dynamical quantities, we consider simple and composite type 2 quenches induced by acting on the initial ground state $|G_\mathrm{i}\rangle = |G_0\rangle$ with the operators

$$\hat{X}^\dagger = \hat{d}^\dagger\,, \quad \hat{Y}_1^\dagger = \hat{c}^\dagger\hat{d}^\dagger\,, \quad \hat{Y}_2^\dagger = \hat{c}\hat{d}^\dagger\,. \tag{38}$$

All three operators describe transitions between the $n_d = 0$ and 1 sectors. The analysis of Sec. II E applies directly, with the identifications $\hat{H}_\mathrm{i} = \hat{H}_0$ and $\hat{H}_\mathrm{f} = \hat{H}_1$, while $\Delta_C = \pm 1$ for $\hat{Y}_1^\dagger$ or $\hat{Y}_2^\dagger$, respectively [see Figs. 1(e)–1(g)]. In particular, Eqs. (27) and (29) imply

$$\mathcal{A}_d(\omega) \sim \omega^{-1+2\eta_d}, \quad \eta_d = \tfrac{1}{2}\Delta_d^2\,, \tag{39a}$$

$$\mathcal{A}_{dc}(\omega) \sim \omega^{-1+2\eta_{dc}}, \quad \eta_{dc} = \tfrac{1}{2}(\Delta_d - 1)^2\,, \tag{39b}$$

$$\mathcal{A}_{dc^\dagger}(\omega) \sim \omega^{-1+2\eta_{dc^\dagger}}, \quad \eta_{dc^\dagger} = \tfrac{1}{2}(\Delta_d + 1)^2\,. \tag{39c}$$

Using NRG, we calculated these three spectra for several values of U [cf. Fig. 2(c)]. In the limit of small ω, the spectra show clear power law behavior, $\omega^{-1+2\eta}$. The exponents η_d, η_{dc}, $\eta_{dc^\dagger}$ extracted from these spectra are shown in Fig. 2(b) (crosses, marked "spec" for "spectra"). They agree well with the values expected (dots, marked "exp" for "expected") from Eqs. (39), based on the value for Δ_d extracted from Eq. (35). Thus all ways of determining Δ_d are completely consistent, confirming the validity of the above analysis.

B. With tunneling: IRLM

The previous section focused on a switch between two sectors of the Hilbert space, with $n_d = 0$ and 1, that were not coupled dynamically, but governed instead by two distinct Hamiltonians, $\hat{H}_\mathrm{i}$ and $\hat{H}_\mathrm{f}$. In the present section, we consider the case that the sectors with $n_d = 0$ and 1 are coupled by tunneling between dot and lead, so that the notion of an initial and final Hamiltonians, acting in decoupled sectors of Hilbert space, does not apply. The dynamics is governed instead by the single Hamiltonian $\hat{H}_\mathrm{i} = \hat{H}_\mathrm{f} = \hat{H}_\mathrm{IRLM}$, given by [see Fig. 3(a)]

$$\hat{H}_\mathrm{IRLM} = \varepsilon_d\,\hat{d}^\dagger\hat{d} \;+ U(\hat{d}^\dagger\hat{d} \;- 1/2)(\hat{c}^\dagger\hat{c} \;- 1/2) + \sum_\varepsilon \varepsilon\,\hat{c}_\varepsilon^\dagger\hat{c}_\varepsilon + \sqrt{\frac{\Gamma}{\pi\rho}}\sum_\varepsilon(\hat{d}^\dagger\hat{c}_\varepsilon + \hat{c}_\varepsilon^\dagger\hat{d})\,. \tag{40}$$

We assume, here and in all later settings, that the hybridization of the dot level with the Fermi sea states is ε independent, with Γ being the bare width of the dot level. Here, in contrast to the local charge model of Eq. (2), the interaction term is taken to be particle-hole symmetric, so that the model is particle-hole symmetric for $\varepsilon_d = 0$.

The presence of the interaction, U, is known to effectively modify the level width,[30,39] both by depleting the electron density in the leads near the dots and thus making tunneling-out easier, and by inducing AO in the leads when the dot occupancy changes. The net result is that the renormalized level width increases with increasing U, and hence is always relevant. A practical way to define the renormalized level width is in terms of the charge susceptibility, $\Gamma_\mathrm{ren} \equiv 1/\pi\chi_c$. For the particle-hole symmetric case considered here (or more generally, for $\varepsilon_d \ll \Gamma_\mathrm{ren}$), the value of Γ_ren (first found in Ref. 39) can be obtained as follows: identify it with the cutoff scale of Eq. (24),

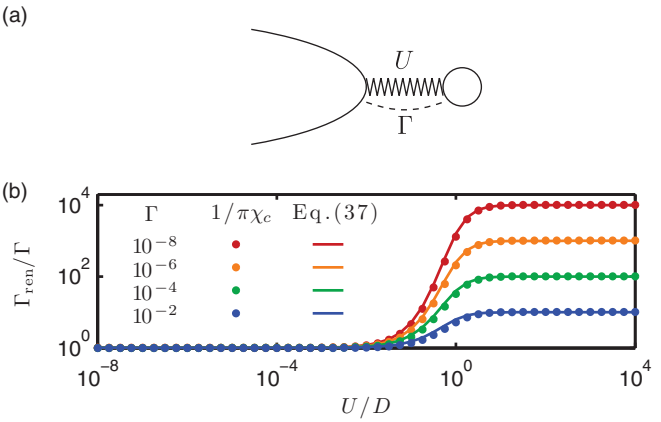

FIG. 3. (Color online) (a) Cartoon of the Hamiltonian (40) for the IRLM. (b) The renormalized level width Γ_ren, calculated via the dot's charge susceptibility, $1/\pi\chi_c$,[30] (dots) or via Eq. (41) (solid line), shown as a function of U for $\varepsilon_d = 0$ and several values of Γ. As U increases from 0, $\Gamma_\mathrm{ren}/\Gamma$ begins to differ significantly from its initial value, namely, 1, only once U becomes comparable to the bandwidth, reaching its maximal value $(\Gamma/D)^{-1/2}$ for $U \gg D$.

$\Gamma_\mathrm{ren} \simeq D^*$, replace η_Y there by $\eta_{dc^\dagger}$ from Eq. (39c), insert $\gamma_Y \propto \sqrt{\Gamma}$ [see Eq. (40)] on the right-hand side of Eq. (24), which gives

$$\Gamma_\mathrm{ren} = D(\Gamma/D)^{1/[2-(1+\Delta_d^\mathrm{ph})^2]}\,, \tag{41}$$

and take

$$\Delta_d^\mathrm{ph} = -\frac{2}{\pi}\tan^{-1}(\pi\rho U/2)\,. \tag{42}$$

Δ_d^ph can be interpreted as the change in scattering phase shift that a system with $\Gamma = 0$, $\varepsilon_d = 0$ experiences if the local occupancy is changed abruptly from $n_d = 0$ to 1. The form of Eq. (42) is analogous to Eq. (37) for Δ_d, with two differences: since the final scattering potentials being compared have amplitude $-U/2$ and $U/2$ (instead of 0 and U), the argument of $\tan^{-1}$ has an extra factor of 1/2, and there is an extra prefactor of 2.

The dependence of Γ_ren on U is illustrated in Fig. 3(b), which shows good agreement between the NRG results for $1/\pi\chi_c$ (dots) and the analytic formula (41) (lines). For U much smaller than the bandwidth D, $\Gamma_\mathrm{ren}/\Gamma$ is essentially equal to 1; it strongly increases once U becomes of the order D, and saturates to $(\Gamma/D)^{-1/2}$ for $U \gg D$.

Let us now consider the equilibrium spectral functions for the operators of Eq. (38), $\mathcal{A}_d^\mathrm{eq}$, $\mathcal{A}_{dc}^\mathrm{eq}$, and $\mathcal{A}_{dc^\dagger}^\mathrm{eq}$. They are defined as in Eq. (26) but with $\hat{H}_\mathrm{f} = \hat{H}_\mathrm{i}$, because for the IRLM, where n_d is not conserved, none of these operators induces a quench. Therefore the $\omega \to 0$ behavior of their correlators is expected (and indeed found) to be independent of AO, since the behavior in this regime is governed by the strong level-environment hybridization fixed point. However, in intermediate frequency regime, $\omega^* < \omega < D$, where $\omega^* \simeq \Gamma_\mathrm{ren}$, the dynamics is governed by the $\Gamma = 0$ LCM fixed point, hence AO behavior still shows up. Intuitively, $1/\omega^*$ corresponds to the time scale within which charge equilibration takes place. Below the energy scale ω^*, the quantum impurity

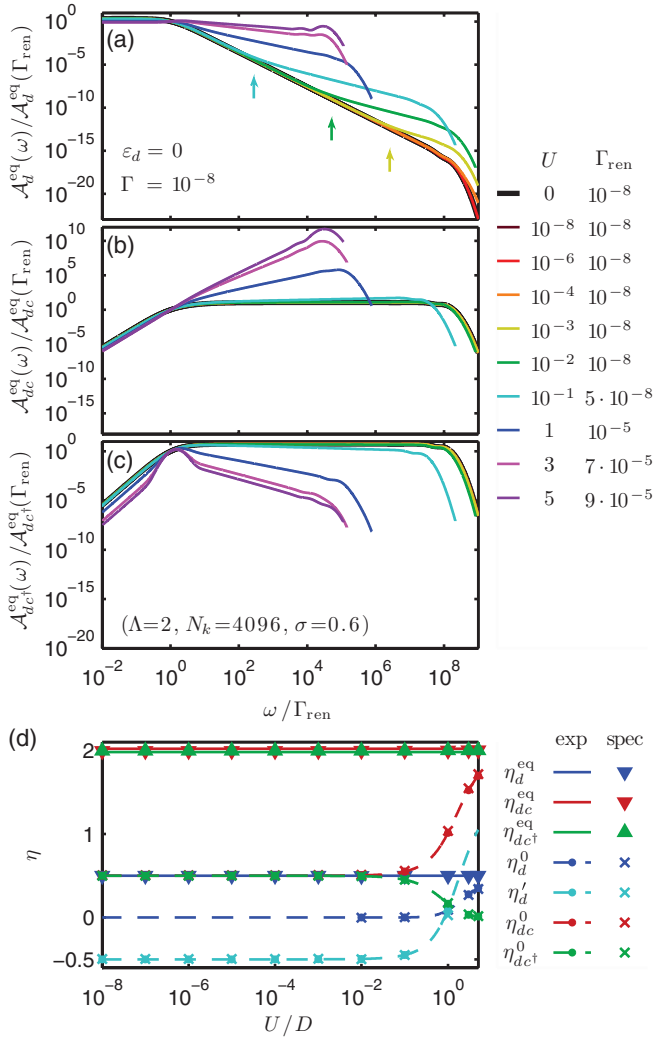

FIG. 4. (Color online) (a)–(c) The equilibrium spectral functions $\mathcal{A}_d^{\rm eq}(\omega)$, $\mathcal{A}_{dc}^{\rm eq}(\omega)$, and $\mathcal{A}_{dc^\dagger}^{\rm eq}(\omega)$ for the IRLM, showing a crossover from trivial power laws, $\omega^{-1+2\eta^{\rm eq}}$, for $\omega<\omega^*$, to AO power laws, $\omega^{-1+2\eta^0}$, for $\omega^*<\omega<D$, with the crossover frequency ω^* given by $\Gamma_{\rm ren}$. (d) Comparison of the exponents $\eta^{\rm eq}$ (triangles) and η^0 or η'_d (crosses) extracted from the spectra shown in (a)–(c), with the values expected from Eqs. (43) for $\eta^{\rm eq}$ (solid lines), and from Eqs. (44) for η^0 or from Eq. (45) for η'_d (dashed lines with dots), for several values of U. In (a), arrows indicate the scale $\bar\omega^*$ that separates the regimes $\omega^*<\omega<\bar\omega^*$ and $\bar\omega^*<\omega<D$, where $\mathcal{A}_d^{\rm eq}$ scales according to Eqs. (45) or (44a), respectively.

becomes strongly correlated with the Fermi sea; above it, tunneling can be treated perturbatively. Let us therefore discuss the two regimes, ω below or above ω^*, separately.

In the regime $\omega\ll\omega^*$, the spectral functions are found to have the following asymptotic form $\mathcal{A}^{\rm eq}\sim\omega^{-1+2\eta^{\rm eq}}$ [cf. Figs. 4(a)–4(c)]:

$$\mathcal{A}_d^{\rm eq}(\omega)\sim\omega^0\,,\quad \eta_d^{\rm eq}=1/2\,, \tag{43a}$$
$$\mathcal{A}_{dc}^{\rm eq}(\omega)\sim\omega^3\,,\quad \eta_{dc}^{\rm eq}=2\,, \tag{43b}$$
$$\mathcal{A}_{dc^\dagger}^{\rm eq}(\omega)\sim\omega^3\,,\quad \eta_{dc^\dagger}^{\rm eq}=2\,. \tag{43c}$$

The exponents arising here can be understood analytically using elementary, though not entirely trivial arguments, based on the fact that at low energies the system is in the vicinity of the fixed point where the level is strongly hybridized with its surroundings, and the lowest-lying excitations of this model have Fermi liquid properties. We refer the reader to Appendix for a detailed analysis. Now consider the regime $\omega^*<\omega<D$, where physics is governed by the LCM (no hybridization) fixed point. As shown in the corresponding regime of $\omega/\Gamma_{\rm ren}>1$ in Figs. 4(a)–4(c), each of the equilibrium spectral functions $\mathcal{A}_d^{\rm eq}$, $\mathcal{A}_{dc}^{\rm eq}$, and $\mathcal{A}_{dc^\dagger}^{\rm eq}$, exhibits another, different power-law there:

$$\mathcal{A}_d^{\rm eq}(\omega)\sim\omega^{-1+2\eta_d^0},\quad \eta_d^0=\tfrac{1}{2}\big(\Delta_d^{\rm ph}\big)^2\,, \tag{44a}$$
$$\mathcal{A}_{dc}^{\rm eq}(\omega)\sim\omega^{-1+2\eta_{dc}^0},\quad \eta_{dc}^0=\tfrac{1}{2}\big(\Delta_d^{\rm ph}-1\big)^2\,, \tag{44b}$$
$$\mathcal{A}_{dc^\dagger}^{\rm eq}(\omega)\sim\omega^{-1+2\eta_{dc^\dagger}^0},\quad \eta_{dc^\dagger}^0=\tfrac{1}{2}\big(\Delta_d^{\rm ph}+1\big)^2\,, \tag{44c}$$

where Eqs. (44b) and (44c) are valid in the entire range $\omega^*<\omega<D$, whereas Eq. (44a) is valid only for $\bar\omega^*<\omega<D$, where $\bar\omega^*>\omega^*$, as we explain below. Remarkably, Eq. (44) have the same form as Eq. (39), except that Δ_d is replaced by $\Delta_d^{\rm ph}$ of Eq. (42), i.e., by the AO exponent involved in abruptly changing the local occupancy from 0 to 1 (in the absence of tunneling). That this exponent should emerge is natural, since the corresponding correlators $\mathcal{G}_d$, $\mathcal{G}_{dc}$, and $\mathcal{G}_{dc^\dagger}$ all involve an operator $d^\dagger$ that places an electron on the dot at time $t=0$. Although the dot occupancy $n_d(t)$ will relax back to its initial value $n_d^{\rm i}$ in the long-time limit, this requires $t\gg1/\omega^*$. In contrast, the lead electrons react to the change in local charge on the much shorter time scale $1/D$. Thus, in the window of intermediate times, $1/D\ll t\ll1/\omega^*$, corresponding to frequencies $\omega^*\ll\omega\ll D$, the situation is similar to that of the previous section, where we had $\Gamma=0$ and a change in dot occupancy from 0 to 1 induced changes in the lead phase shifts, accompanied by AO. Thus the exponents η^0 arising in Eq. (44) can be identified as the (equilibrium) scaling dimensions of the corresponding operators calculated in the *absence* of tunneling (which is why we use a superscript 0 on such exponents, here and below). This explains the similarity between the behavior described by Eqs. (44) and (39). Note that the scaling dimension $\eta_{dc^\dagger}^0$ [see Eq. (44c)] of the tunneling operators $\hat d\hat c^\dagger$ and $\hat c^\dagger\hat d$ satisfy $0\leqslant\eta_{dc^\dagger}^0\leqslant1/2$ [since for $U>0$, we have $-1\leqslant\Delta_d^{\rm ph}\leqslant0$, by Eq. (42)], thus tunneling is always relevant around the LCM fixed point for this model.

As was mentioned above, the power law (44a) describing the increase of $\mathcal{A}_d^{\rm eq}(\omega)$ with decreasing ω is not valid for the entire high-frequency range $\omega^*<\omega<D$, but only for its upper subrange $\bar\omega^*<\omega<D$, with $\omega^*<\bar\omega^*$. The reason is that $\mathcal{A}_d^{\rm eq}(\omega)$ contains another contribution, to be called "sub-Lorentzian," that grows more rapidly than Eq. (44a) with decreasing ω, causing a crossover to the form:

$$\mathcal{A}_d^{\rm eq}(\omega)\sim\omega^{-1+2\eta'_d}\,,\quad \eta'_d=-\tfrac{1}{2}-\Delta_d^{\rm ph}+\big(\Delta_d^{\rm ph}\big)^2\,, \tag{45}$$

in the range $\omega^*<\omega<\bar\omega^*$. The origin of this non-AOC contribution can be understood by analyzing the behavior predicted by the LCM fixed point (no hybridization, $\Gamma=0$) in the noninteracting limit, $U=0$. In this limit, $\mathcal{A}_{d,U=0}^{\rm eq}(\omega)$ reduces to the δ-function density of states of a noninteracting resonant level disconnected from the environment: indeed, Eq. (44a) yields $\mathcal{A}_{d,U=0}^{\rm eq}(\omega)\sim\omega^{-1}$, which corresponds to the imaginary part of $(\omega+i0^+)^{-1}$ [Eq. (44a) does not specify the

prefactor, though, which in this limit is 0^+, i.e., infinitesimally small]. Since $\mathcal{A}^{\rm eq}_{d,U=0}(\omega)$ has no support at high frequencies for $\Gamma = 0$, it is sensitive to the effects of finite Γ, which turns it into a Lorentzian [see Eq. (A2) of Appendix] that decays as ω^{-2}. Now, when interactions are turned on, $U \neq 0$, two changes occur. First, the tails of the Lorentzian are modified[40,41] to take the sub-Lorentzian form (45), which decays somewhat slower than ω^{-2} (since η'_d is less negative than $-\frac{1}{2}$). Second, $\mathcal{A}^{\rm eq}_{d,U\neq 0}(\omega)$ acquires an AOC term of the form Eq. (44a), which now contributes to the high-frequency behavior. Since its exponent is η^0_d is less negative than η'_d, the AOC contribution decays more slowly than the sub-Lorentzian contribution and hence will dominate for sufficiently large ω. Thus there will be a crossover scale, $\bar{\omega}^*$ [marked by arrows in Fig. 4(a)], such that the AOC behavior (44a) holds for $\bar{\omega}^* < \omega < D$ while the sub-Lorentzian behavior (45) holds for $\omega^* < \omega < \bar{\omega}^*$. For $U = 0$, the crossover scale is given by $\bar{\omega}^* = D$, as explained above. It decreases with increasing U, as seen in Fig. 4(a), and drops below ω^* when U becomes of order D. The exponent η'_d becomes less negative with increasing U, but remains close to its $U = 0$ value of $-\frac{1}{2}$ (implying nearly Lorentzian ω^{-2} tails) as long as $U \ll D$, as seen in Fig. 4(d). When U passes D, η'_d increases past η^0_d, but at that point, the frequency window $\omega^* < \omega < \bar{\omega}^*$ has already shrunk to zero. In contrast to $\mathcal{A}^{\rm eq}_d(\omega)$, the spectral functions $\mathcal{A}^{\rm eq}_{dc}(\omega)$ and $\mathcal{A}^{\rm eq}_{dc^\dagger}(\omega)$ do have nonvanishing high frequency tails even for $U = 0$ and $\Gamma = 0$, which evolve into the AOC behavior for $U \neq 0$. Thus, the analog of the "Lorentzian tail" is always subleading, so that a scale corresponding to $\bar{\omega}^*$ does not show up and Eqs. (44b) and (44c) are valid in the entire range $\omega^* < \omega < D$. Finally, we mention that $\mathcal{A}^{\rm eq}_{dc^\dagger}(\omega)$ contains a δ peak of the form $a\,\delta(\omega)$, with weight $a = |\langle G_{\rm i}|\hat{d}\hat{c}^\dagger|G_{\rm i}\rangle|^2$. This follows from its Lehmann representation of the form (28b), because the ground-state expectation value of $\hat{d}\hat{c}^\dagger$ is nonzero. [Since the latter statement does not hold for $\hat{d}$ and $\hat{c}\hat{d}$, which do not conserve particle number, the corresponding spectral functions $\mathcal{A}^{\rm eq}_c(\omega)$ and $\mathcal{A}^{\rm eq}_{dc}(\omega)$ lack a $\delta(\omega)$ contribution.] The δ-function peak in $\mathcal{A}^{\rm eq}_{dc^\dagger}(\omega)$ is, however, unrelated to AOC physics, and hence will not be discussed any further. [Similar $\delta(\omega)$-function peaks occur for some of the other equilibrium spectral functions discussed further below, but they will likewise be ignored in the present paper.]

C. Quantum quench of level position

In the previous section, we emphasized the importance of the scale ω^*, which separates the low- and intermediate-frequency regimes, showing trivial exponents or AO exponents, respectively. It is instructive to study the role of the scale ω^* in a slightly different but related context, namely, quench spectral functions involving a quantum quench of the level position. This will shed further light on the AO between states with different local level occupancies.

Concretely, we consider initial and final Hamiltonians that both are of the form Eq. (40), but with initial and final level positions that are symmetrically spaced on opposite sides of the model's symmetry point at $\varepsilon_d = 0$:

$$\varepsilon_d^{\rm i} = W/2 \quad \stackrel{\text{quench}}{\longrightarrow} \quad \varepsilon_d^{\rm f} = -W/2\,. \tag{46}$$

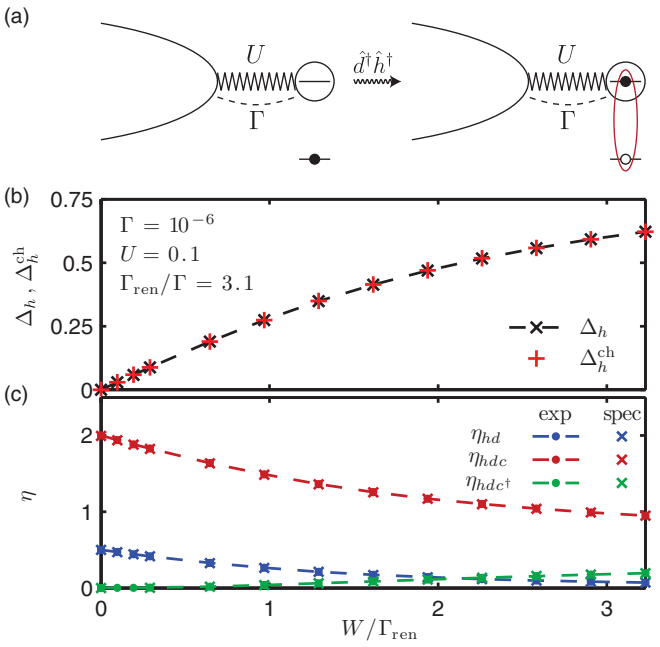

FIG. 5. (Color online) (a) Cartoon of the quench which occurs when an electron-hole pair is created at time $t = 0$, see Eq. (47). (The cartoon depicts the situation relevant for exciton creation by absorption of a photon, which excited an electron from a valence-band to a conduction band level of a semiconducting quantum dot.) (b) The exponent Δ_h [from Eq. (11)] and the displaced charge $\Delta_h^{\rm ch}$ [from Eq. (12)], for the quench of Eq. (46), as a function of the quench range W. (c) Corresponding values of the AO exponents η_{hd}, η_{hdc}, and $\eta_{hdc^\dagger}$, extracted from the asymptotic behavior $\omega^{-1+2\eta}$ of spectral functions (crosses), or as expected from Eqs. (50) (dots). Typically, relative errors are less than 1%.

Although this is an example of a type 1 quench, it will be convenient (mainly for notational reasons) to reformulate this situation as a type 2 quench. To this end, we use the Hamiltonian

$$\hat{H} = W(1/2 - \hat{n}_h)\hat{n}_d + U(\hat{n}_d - 1/2)(\hat{c}^\dagger\hat{c} - 1/2) + \sum_\varepsilon \varepsilon\,\hat{c}^\dagger_\varepsilon\hat{c}_\varepsilon + \sqrt{\frac{\Gamma}{\pi\rho}}\sum_\varepsilon(\hat{d}^\dagger\hat{c}_\varepsilon + \hat{c}^\dagger_\varepsilon\hat{d})\,, \tag{47}$$

where we have introduced an auxiliary degree of freedom, called "hole" (in analogy to the role of holes in exciton creation by optical absorption),[14–16] with hole counting operator $\hat{n}_h = \hat{h}^\dagger\hat{h}$. The hole has no dynamics; its only role is to distinguish two distinct sectors of Hilbert space in which the dynamics is described by $\hat{H}_{\rm i}$ or $\hat{H}_{\rm f}$, with hole number $n_h = 0$ or 1, respectively [see Fig. 5(a)]. The type 2 quench that switches between these sectors is induced by $\hat{X}^\dagger = \hat{h}^\dagger$. The overlap $\mathcal{O}_h \sim N^{-\frac{1}{2}\Delta_h^2}$ between the initial and final ground states is characterized by an AO exponent Δ_h [see Eq. (11)] that is equal to the charge $\Delta_h^{\rm ch}$ displaced by the quench [see Eq. (12)].

The magnitude of Δ_h increases with the range W of the quench, as shown in Fig. 5(b) (linear scale) and Fig. 6(a) (log-log scale). Note, in particular, that the scale on which the quenching range W needs to change in order for the AO exponents to change significantly, is given by $\Gamma_{\rm ren}$. This is natural: when $W \gg \Gamma_{\rm ren}$, the two states $|G_{\rm i}\rangle$ and $|G_{\rm f}\rangle$

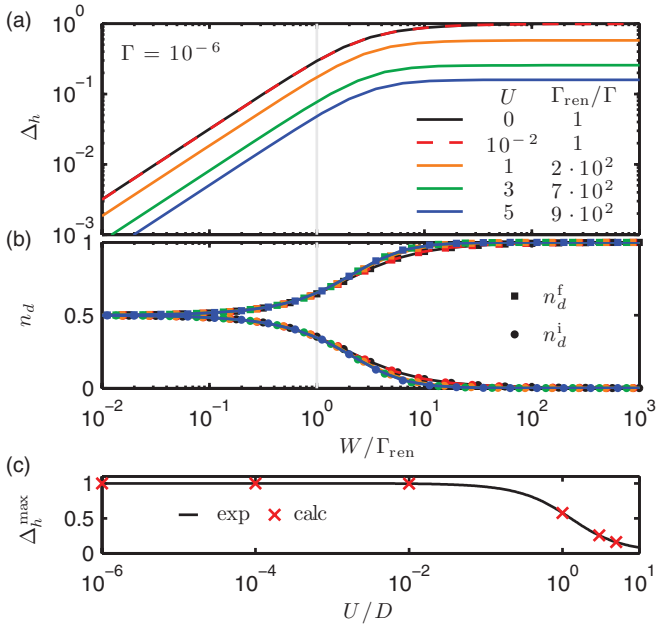

FIG. 6. (Color online) (a) The AO exponent Δ_h [extracted according to Eq. (11)] as a function of $W/\Gamma_{\rm ren}$ for several values of U. For $W/\Gamma_{\rm ren} \gg 1$, Δ_h approaches its maximal value $\Delta_h^{\rm max}$. As W is reduced below $\Gamma_{\rm ren}$, Δ_h drops below its maximal value and decreases with W [linearly so for $W/\Gamma_{\rm ren} \ll 1$]. (b) The final and initial occupancies $n_d^{\rm f}$ (squares, upper curves) and $n_d^{\rm i}$ (circles, lower curves) as functions of $W/\Gamma_{\rm ren}$ for the same values of U [same color code as in (a)]. (c) The maximal value $\Delta_h^{\rm max}$ of the AO exponent Δ_h, extracted from the $W/\Gamma_{\rm ren} \gg 1$ regime of (a) (crosses, "calc"), or expected from Eq. (48) (solid line, "exp"); the relative deviations are well below 1%.

connected by the quench describe dots with strongly different occupancies, $n_d^{\rm i} \simeq 0$ versus $n_d^{\rm f} \simeq 1$, see Fig. 6(b). Hence the AO [see Eq. (11)] of the corresponding Fermi seas will be strong. The maximum possible value of the exponent Δ_h is

$$\Delta_h^{\rm max} = 1 + \Delta_d^{\rm ph}\,, \tag{48}$$

with $\Delta_d^{\rm ph}(U) < 0$ given by Eq. (42). The first term simply gives the $U \to \infty$ value of the change in dot occupancy induced by the quench, namely, 1; the second term reflects the reaction of the Fermi sea to this change, cf. Sec. III B.

Following the arguments of Sec. II E, the nonequilibrium spectral functions $\mathcal{A}_Y(\omega)$, defined for

$$\hat{Y}_1^\dagger = \hat{d}^\dagger \hat{h}^\dagger\,, \quad \hat{Y}_2^\dagger = \hat{c}^\dagger \hat{d}^\dagger \hat{h}^\dagger\,, \quad \hat{Y}_3^\dagger = \hat{c}\,\hat{d}^\dagger \hat{h}^\dagger\,, \tag{49}$$

are expected to show the following AO behavior for $\omega \to 0$:

$$\mathcal{A}_{hd}(\omega) \sim \omega^{-1+2\eta_{hd}}, \quad \eta_{hd} = \tfrac{1}{2}(\Delta_h - 1)^2\,, \tag{50a}$$

$$\mathcal{A}_{hdc}(\omega) \sim \omega^{-1+2\eta_{hdc}}, \quad \eta_{hdc} = \tfrac{1}{2}(\Delta_h - 2)^2\,, \tag{50b}$$

$$\mathcal{A}_{hdc^\dagger}(\omega) \sim \omega^{-1+2\eta_{hdc^\dagger}}, \quad \eta_{hdc^\dagger} = \tfrac{1}{2}\Delta_h^2\,. \tag{50c}$$

The reason for the specific form of the exponents is that for the correlators $\mathcal{G}_{hd}$, G_{hdc}, or $G_{hdc^\dagger}$ at $t = 0$, the local charge (on the d level or in the Fermi sea) is increased by one, two, or zero, respectively [i.e., $\Delta_C = 1$, 2, or 0 in Eq. (16)]. Figure 5(c) shows that the exponents (crosses) extracted from the asymptotic behaviour $\mathcal{A}_Y(\omega)$ are indeed in good agreement with values expected (dots) from Eq. (50).

IV. POPULATION SWITCHING WITHOUT SENSOR

The models investigated so far served as testing ground for the influence of AO on various types of spectral functions. The following two sections have the concrete motivation to clarify the role of AO in the context of quantum dot models that display the phenomenon of population switching (PS).[17,18,32,33,42–47] In such models, a quantum dot, tunnel coupled to leads, contains levels of different widths and is capacitively coupled to a gate voltage that shifts the levels energy relative to the Fermi level of the leads. Under suitable conditions, an (adiabatic) sweep of the gate voltage induces an inversion in the population of these levels (a so-called population switch), implying a change in the local potential seen by the Fermi seas in the leads. Goldstein, Berkovits, and Gefen (GBG) have argued in Refs. 17 and 18 that in this context, AO can play an important role. In particular, they pointed out that for a model involving a third lead acting as a charge sensor, the effects of AO can be enhanced to such an extent that population switching becomes abrupt, i.e., turns into a phase transition. Our goal is to elucidate the influence of AO by using the tools developed above in the context of the IRLM.

In the present section, we will study population switching in a two-lead model (without charge sensor), which is equivalent to an anisotropic Kondo model.[17,18,48–51] The corresponding Kondo temperature, $T_{\rm K}$, sets the width of the population switch as a function of gate voltage. We calculate the spectral function $\mathcal{A}_Y^{\rm eq}(\omega)$ of the pseudospin-flip operator and show that $T_{\rm K}$ also acts as the crossover scale ω^* that separates a low-frequency regime showing Fermi-liquid power laws from an intermediate-frequency regime revealing AO exponents. We investigate the origin of the latter by a quantum quench analysis similar to that of Sec. III C above. In the following section, we will generalize the model by adding a charge sensor and analyze how this enhances the effects of AO.

A. Width of switching regime

We consider a model involving two single-level dots ($\mu = {\rm L,R}$) and, for convenience, choose their level energies ε_d to be equal, so that the PS always occurs at the particle-hole symmetric point, $\varepsilon_d = -U/2$. (Note that PS occurs also for nondegenerate levels, as long as their level spacing is smaller than the difference of their level widths Γ_μ.) The levels have an electrostatic coupling $U > 0$ and are each tunnel coupled to its own lead [see Fig. 7(a)]:

$$\hat{H}_{\rm SIAM} = \sum_\mu \varepsilon_d\, \hat{d}_\mu^\dagger \hat{d}_\mu + U \hat{d}_{\rm L}^\dagger \hat{d}_{\rm L} \hat{d}_{\rm R}^\dagger \hat{d}_{\rm R} + \sum_{\varepsilon\mu} \varepsilon\, \hat{c}_{\varepsilon\mu}^\dagger \hat{c}_{\varepsilon\mu} + \sum_\mu \sqrt{\frac{\Gamma_\mu}{\pi\rho}} \sum_\varepsilon (\hat{d}_\mu^\dagger \hat{c}_{\varepsilon\mu} + \hat{c}_{\varepsilon\mu}^\dagger \hat{d}_\mu). \tag{51}$$

(We use notation analogous to that of Sec. III B.) We choose the level widths to be strongly asymmetric and will use a fixed value of their ratio, $\Gamma_{\rm R}/\Gamma_{\rm L} = 20$, throughout. The model thus

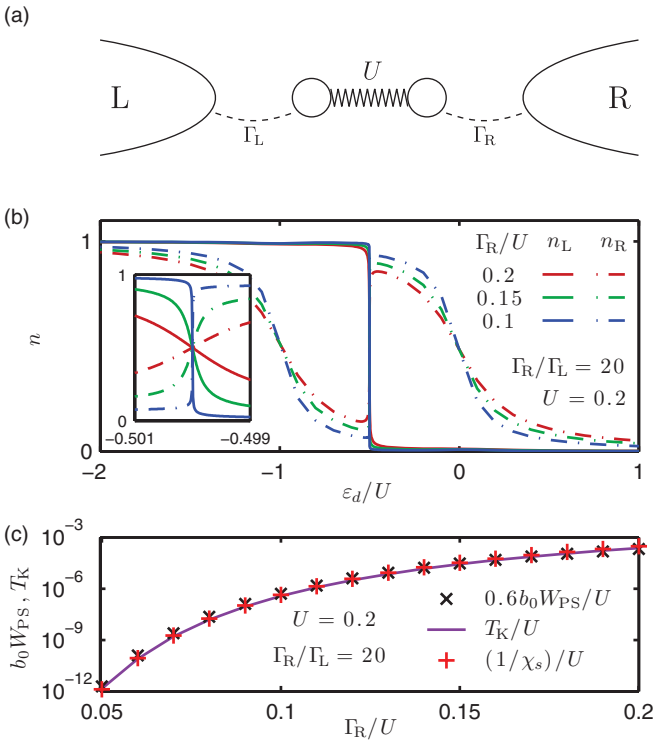

FIG. 7. (Color online) (a) Cartoon of the Hamiltonian (51) for the asymmetric SIAM. (b) The occupations n_L (solid lines) and n_R (dashed lines) of the left and right levels, respectively, as functions of ε_d, for several values of Γ_R, at a fixed ratio of $\Gamma_R/\Gamma_L = 20$. As ε_d is lowered past the particle-hole symmetric point at $\varepsilon_d = -U/2$, population switching occurs, with n_R changing from near 1 to near 0, and vice versa for n_L. Inset: zoom into the switching region around $\varepsilon_d = -U/2$, showing that the switch is continuous (as a function of ε_d) even though the switching region becomes narrower for decreasing Γ_R. (c) Comparison of $b_0 W_{PS}$ [from Eqs. (52) and (56), crosses], T_K [from Eq. (57), solid], and the inverse pseudospin susceptibility $1/\chi_s$ (pluses). All three quantities evidently decrease similarly with decreasing Γ_R/U.

has the form of a spin-asymmetric single-impurity Anderson model (SIAM), where μ acts as pseudospin index.

As illustrated in Fig. 7(b), this model shows PS when ε_d is decreased past $\varepsilon_d = -U/2$ (the particle-hole symmetric point): as this "switching point" is crossed, the occupancy of the broad level (dashed lines) changes from near 1 to near 0, and vice versa for the narrow level (solid lines). We define the width of the switching regime W_{PS} as the difference,

$$W_{PS} \equiv \varepsilon_d(n_{R+}) - \varepsilon_d(n_{R-}) , \tag{52}$$

between those two values of ε_d, located symmetrically on either side of the switching point, at which the occupation of the right level is $n_{R+} \equiv \frac{3}{4} n_{R+}^{max}$ ($> \frac{1}{2}$) or $n_{R-} = 1 - n_{R+}$ ($< \frac{1}{2}$), respectively, where n_{R+}^{max} is the largest value reached by n_R for $\varepsilon_d > -U/2$, to the right of the PS.

Figure 7(b) and its inset show that the width of the switching regime decreases with decreasing Γ_μ, without, however, dropping to zero as long as the level widths are nonzero. This behavior can be understood as follows.[17,18,48–51] In the vicinity of the particle-hole symmetric point, only two local charge configurations are relevant, namely those with occupancies (n_L,n_R) equal to (0,1) or (1,0). The spin-asymmetric SIAM can thus be mapped onto an anisotropic Kondo model by a Schrieffer-Wolff transformation. This leads to an anisotropic pseudospin exchange interaction of the form

$$\hat{H}_{exch} = \frac{J_z}{4}(\hat{d}_L^\dagger \hat{d}_L - \hat{d}_R^\dagger \hat{d}_R)(\hat{c}_L^\dagger \hat{c}_L - \hat{c}_R^\dagger \hat{c}_R) + \frac{J_{xy}}{2}(\hat{c}_L \hat{c}_R^\dagger \hat{d}_L^\dagger \hat{d}_R + \text{H.c.}) + B_{eff}(\hat{d}_L^\dagger \hat{d}_L - \hat{d}_R^\dagger \hat{d}_R)/2 , \tag{53}$$

respectively, with coupling constants given by

$$J_z = U_L + U_R, \quad J_{xy} = 2\sqrt{U_L U_R} , \tag{54}$$

where

$$\rho U_\mu = \frac{\Gamma_\mu}{\pi}\left(\frac{1}{\varepsilon_d + U} + \frac{1}{|\varepsilon_d|}\right) \tag{55}$$

and effective magnetic field

$$B_{eff} = b_0(\varepsilon_d + U/2), \quad b_0 = \frac{4(\Gamma_R - \Gamma_L)}{\pi U} . \tag{56}$$

Since $\Gamma_R \gg \Gamma_L$ in our system, the Kondo model is highly anisotropic, $J_z \gg J_{xy}$. The corresponding Kondo temperature is given by the following expression [see also Eq. (59) below]:[48,52]

$$T_K = \frac{\sqrt{U(\Gamma_L + \Gamma_R)}}{\pi} \exp\left[\frac{\pi \varepsilon_d(U + \varepsilon_d)}{2U(\Gamma_L - \Gamma_R)} \ln \frac{\Gamma_L}{\Gamma_R}\right] . \tag{57}$$

Note that T_K decreases exponentially if Γ_μ is decreased with a fixed ratio of Γ_R/Γ_L and actually becomes zero for $\Gamma_\mu = 0$ (the argument of the exponent in Eq. (57) is negative, since $\varepsilon_d < 0$).

Now, T_K can be associated with the energy gained by forming a ground state involving a screened local pseudospin, which in the present setting, translates to a ground state involving a coherent superposition of configurations with local occupancies (0,1) and (1,0). Screening will cease when ε_d deviates sufficiently from the symmetry point $-U/2$ that the effective magnetic field $|B_{eff}|$ exceeds T_K, in which case the ground state will be dominated solely by the (0,1) or (1,0) configuration, instead of involving a coherent superposition of both. Thus the switching width will be set by $b_0 W_{PS} \simeq T_K$, up to a numerical constant of order unity.

Figure 7(c) confirms this expectation. It shows that b_0 times the switching width W_{PS} [from Eq. (52)] (crosses) and the Kondo temperature T_K at $\varepsilon_d = -U/2$ [from Eq. (57)] (solid line), when plotted as functions of Γ_R/U at fixed Γ_R/Γ_L, are indeed almost perfectly proportional to each other. As a numerical consistency check, Fig. 7(c) also shows the inverse of the zero-temperature pseudospin susceptibility of the dot levels, $1/\chi_s$ (pluses), confirming that $T_K = 1/\chi_s$. (This is analogous to the relation $\Gamma_{ren} = 1/\pi\chi_c$ of Sec. III B.)

B. AO in dynamics of pseudospin-flip operator

Let us now explore the role of AO in population switching. To this end, we note that the effective exchange interaction $\hat{H}_{exch}$ of Eq. (53) is similar in structure to the IRLM of Eq. (40): both involve two charge configurations [(0,1) and (1,0) for Eq. (53), or 0 and 1 for Eq. (40)], which induce different

phase shifts in the leads due to a dot-lead interaction term (parametrized by J_z in the former and U in the latter) and which are connected by a tunneling term (parametrized by J_{xy} in the former, Γ in the latter). More formally, the relation between the IRLM and PS is revealed by the equivalence of both models to the Kondo model (for the IRLM, this equivalence is discussed, e.g., in Refs. 13, 30, and 39). Thus we may expect AO to play a similar role for both models, and hence perform an analysis similar to that in Secs. III B and III C.

Specifically, since by Eqs. (54) and (55) $J_{xy} \ll J_z$, let us study the spectral function $\mathcal{A}_Y^{\rm eq}(\omega)$ of the pseudospin-flip operators occurring in $\hat{H}_{\rm exch}$,

$$\hat{Y}^\dagger = \hat{c}_{\rm L}\hat{c}_{\rm R}^\dagger\hat{d}_{\rm L}^\dagger\hat{d}_{\rm R}\,, \quad \hat{Y} = \hat{d}_{\rm R}^\dagger\hat{d}_{\rm L}\hat{c}_{\rm R}\hat{c}_{\rm L}^\dagger\,. \tag{58}$$

These induce transitions between the local charge configurations (0,1) and (1,0) and simultaneously add an electron to one lead while removing an electron from the other. (Such a transition does not constitute a quench, since for the present model, n_d is not conserved.) $\mathcal{A}_Y^{\rm eq}$ should, in some respects, be analogous to $\mathcal{A}_{dc^\dagger}$ of Sec. III B. We have thus calculated $\mathcal{A}_Y^{\rm eq}$ numerically, using the Hamiltonian $\hat{H}_{\rm SIAM}$ of Eq. (51). Indeed, Fig. 8(a), which shows $\mathcal{A}_Y^{\rm eq}(\omega)$ for several values of $\Gamma_{\rm R}/U$, exhibits several features reminiscent of Fig. 4(c) for $\mathcal{A}_{dc^\dagger}(\omega)$. (i) Since $\hat{Y}$ is relevant at the $J_{xy} = 0$ fixed point, having there a scaling dimension $\eta_Y^0 < 1$ [cf. Eq. (61b) below], there exists a crossover scale ω^*, separating a regime intermediate frequencies, where the system is effectively close to the $J_{xy} = 0$ fixed point, and a regime of very low frequencies, where the system is governed by strong pseudospin-screening fixed point. Equation (24) then implies

$$\omega^* \simeq \omega_{\rm he}\left(\frac{J_{xy}}{\omega_{\rm he}}\right)^{1/(1-\eta_Y^0)}\,, \tag{59}$$

where $\omega_{\rm he}$ is a high-energy scale set by the minimum of the bandwidth or the cost of local charge fluctuations. By Eqs. (54), (55), and (61b), ω^* is nothing else but the Kondo temperature (57), in the limit $\Gamma_{\rm R} \gg \Gamma_{\rm L}$ addressed here. (ii) When properly rescaled by plotting $\mathcal{A}_Y^{\rm eq}(\omega)/\mathcal{A}_Y^{\rm eq}(\omega^*)$ versus ω/ω^*, all curves collapse onto each other in the regime $\omega \lesssim D$. (iii) In the low-frequency regime $\omega \ll \omega^*$, we find the same Fermi-liquid power law (dotted line)

$$\mathcal{A}_Y^{\rm eq}(\omega) \sim \omega^3\,, \quad \omega \ll \omega^*\,, \tag{60}$$

dictated by the pseudospin screening fixed point, as for $\mathcal{A}_{dc^\dagger}(\omega)$ [cf. Eq. (43c)]. (An analytical explanation for this fact is given at the end of Appendix.) (iv) In an intermediate-frequency regime $\omega^* \lesssim \omega \lesssim \omega_{\rm he}$, i.e., in the vicinity of the $J_{xy} = 0$ fixed point, we find an AO-dominated power law:

$$\mathcal{A}_Y^{\rm eq}(\omega) \sim \omega^{-1+2\eta_Y^0}, \quad \omega^* \lesssim \omega \lesssim \omega_{\rm he}\,. \tag{61a}$$

Indeed, though the numerical calculation of $\mathcal{A}_Y^{\rm eq}(\omega)$ was performed using the full Hamiltonian $\hat{H}_{\rm SIAM}$ of Eq. (51), tunneling is not important on the short time scales that govern the frequency regime $\omega > \omega^*$. Hence we expect the exponent η_Y^0 found from Eq. (61a) to be equal in value to that which one would obtain in the $\omega \to 0$ limit of a calculation performed in the *absence* of pseudospin flips, i.e., using $\hat{H}_{\rm exch}$ with $J_{xy} = 0$.

In the absence of pseudospin flips, the correlator involving $\hat{Y}$ would actually constitute a type 2 quench correlator, because

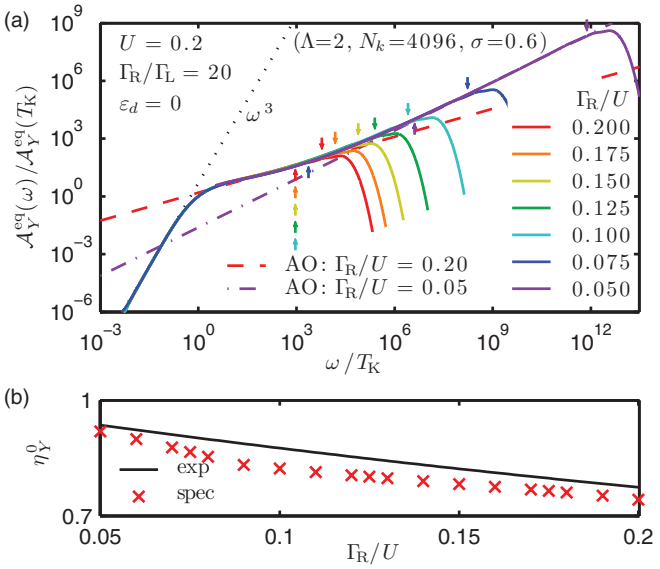

FIG. 8. (Color online) (a) The pseudospin-flip spectral function $\mathcal{A}_Y^{\rm eq}(\omega)$ [cf. Eq. (58)] for the PS model without charge sensor, for several values of $\Gamma_{\rm R}/U$ with fixed ratio $\Gamma_{\rm R}/\Gamma_{\rm L}$, calculated at $\varepsilon_d = -U/2$: plotting $\mathcal{A}_Y^{\rm eq}(\omega)/\mathcal{A}_Y^{\rm eq}(T_{\rm K})$ versus $\omega/T_{\rm K}$ yields a scaling collapse. The frequency dependence of the curves qualitatively changes at $T_{\rm K}$; for $\omega < T_{\rm K}$, we find Fermi-liquid behavior, $\sim\omega^3$ (dotted line), while for $\omega > T_{\rm K}$, each curve shows a nontrivial AO power law, $\sim\omega^{-1+2\eta_Y^0}$ [see Eq. (61)], exemplified by the dashed and dash-dotted lines for $\Gamma_{\rm R}/U = 0.2$ and 0.05, respectively. (b) Comparison of the values for η_Y^0 expected from Eq. (61b) (solid line), or extracted from the spectral function $\mathcal{A}_Y^{\rm eq}(\omega)$ (crosses) by fitting Eq. (61a) to it in the intermediate-frequency regime between $T_{\rm K}$ and the high-frequency maximum. For each curve in panel (a), two arrows of corresponding color above and below the curve, indicate the fitting range's upper and lower ends, respectively. None of the fitting ranges extend below $10^3 T_{\rm K}$ (hence the accumulation of arrows there), since below this value the logarithmic corrections discussed in the text become significant, causing the curves to bend. The effect of these logarithmic corrections increases with increasing $\Gamma_{\rm R}/U$, since this reduces the width of the fitting range [see (a)], causing the relative error between crosses and solid line to increases from 1% for $\Gamma_{\rm R}/U = 0.05$ to 10% for $\Gamma_{\rm R}/U = 0.2$.

$\hat{Y}^\dagger$ changes $(\hat{n}_{\rm L} - \hat{n}_{\rm R})$, which is a conserved quantum number for Hamiltonians without pseudospin flips. Therefore the expected value of η_Y^0 can be predicted using the generalized Hopfield rule [Eq. (29)]. For the present case of two channels that are not interconnected by tunneling, so that the total charge within each channel is conserved, it can be applied to each channel separately, adding the corresponding exponents[21] [cf. Eq. (31)]:

$$\eta_Y^0 = \tfrac{1}{2}(\Delta_{\rm L} + 1)^2 + \tfrac{1}{2}(-\Delta_{\rm R} - 1)^2\,. \tag{61b}$$

Here, Δ_μ describes the change in phase shift, divided by π, induced in lead μ by a pseudospin flip; it is given by Eq. (42), with U replaced by U_μ [from Eq. (55)]. The applicability of these arguments is confirmed by Fig. 8(b), which shows that the exponents extracted from the numerical spectra (crosses) agree quite well with the values expected from Eq. (61b) (solid line).

The agreement is not perfect, though, and deteriorates with increasing Γ_R/U, i.e., with increasing $\omega^* \simeq T_K$. To understand this, recall that the AO power law results from analyzing the RG equations to lowest-order approximation in J_{xy}. To that order, the simple RG Eq. (23) is valid, and renormalization of J_z (and therefore of η_Y^0) is negligible. As full Kondo RG equations show, this requires $J_z \gg J_{xy}$, or more accurately $(J_z/J_{xy})^2 \gg 1$.[25] Subleading terms cause logarithmic corrections in $1/\ln(\omega/T_K)$. In our studies, we used a fixed ratio of $(J_z/J_{xy})^2 \simeq 5.5$ [cf. Eqs. (54) and (55)], which is not large enough for the logarithmic corrections to be entirely negligible. Thus pure AOC behavior can be expected only at the high-frequency end of the range $\omega^* < \omega < D$, while deviations from AOC behavior should become noticeable as ω decreases and becomes closer to ω^*. Indeed, this expectation is borne out in Fig. 8(a) in which the fitting ranges used are marked by arrows: the best AOC behavior (straightest line on log-log plot) is found at high frequencies for the smallest values of Γ_R/U for which the range $\omega^* < \omega < D$ is widest. However, with increasing Γ_R/U, which increases ω^* and hence reduces the range $\omega^* < \omega < D$, the AOC and non-AOC behaviors become increasingly harder to separate, resulting in the deviations, evident in Fig. 8(b), between the exponent extracted numerically and predicted analytically. Up to the caveat just discussed (which would disappear in the limit $\Gamma_R/\Gamma_L \gg 1$), Eq. (61b) allows us to understand why PS is always continuous in this model: since $-1 \leqslant \Delta_\mu \leqslant 0$, the scaling dimension of $\hat{Y}$ satisfies $\eta_Y^0 \leqslant 1$, as mentioned above, implying that this operator always remains a relevant perturbation around the $J_{xy} = 0$ fixed point, and does not flow to zero at low-energy scales. This means that AO, although present, is not strong enough to completely suppress the amplitude for pseudospin-flip transitions. Hence, the two sectors (0,1) and (1,0) are always coupled by the effective low-energy Hamiltonian, so that population switching is continuous.[17,18]

C. AO induced by quench of level positions

As mentioned above, the operators $\hat{Y}^\dagger$ and $\hat{Y}$ connect two configurations with different local occupancies, (0,1) and (1,0). To shed further light on the AO between such configurations, we now perform a quantum quench analysis similar to that of Sec. III C. We consider a type 1 quench, $\hat{H}_i \to \hat{H}_f$, induced by changing the level position ε_d from a value above the symmetry point, favoring (0,1), to one below, favoring (1,0):

$$\varepsilon_d^i = -U/2 + W/2 \quad \overset{\text{quench}}{\longrightarrow} \quad \varepsilon_d^f = -U/2 - W/2\,. \quad (62)$$

The corresponding ground states, $|G_i\rangle$ and $|G_f\rangle$, will display AO as in Eq. (1). Based on the lessons learnt from Sec. III C, the corresponding exponent Δ_{AO} will increase with the width W of the quench. Indeed, Fig. 9 [to be compared with Fig. 6(a)] shows that Δ_{AO} increases from close to 0 for W much below T_K/b_0 (indicated by vertical dashed lines) to a maximal value of

$$\Delta_{AO}^{\max} = \sqrt{(1)^2 + (1)^2} = \sqrt{2} \quad (63)$$

for $W \gg T_K/b_0$. This maximal value reflects the displaced charge Δ_{ch} [cf. Eq. (7)] induced by a very strong quench: both n_L and n_R are $\simeq 0$ (or $\simeq 1$) if the level position is far above (or below) the Fermi energy, $\varepsilon_d^i = -U/2 + W/2 \gg 0$ (or $\ll 0$), cf. Fig. 7(b), thus the displaced charge associated with both n_L and n_R is 1. (The contribution to Δ_{ch} from the leads turns out to be negligible here,[21] since for sufficiently large W, the Fermi sea is essentially decoupled from the dot.)

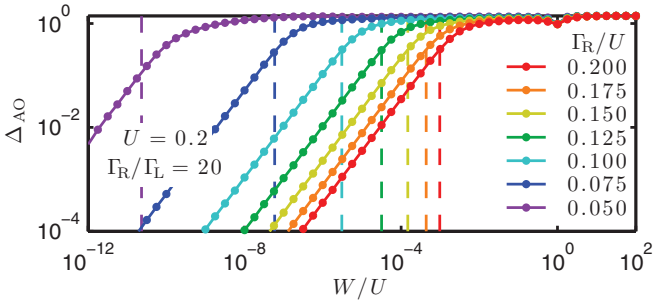

FIG. 9. (Color online) AO for the PS model without charge sensing. The exponent Δ_{AO} [extracted from Eq. (1)] (solid lines with dots) is shown as function of quench size W/U [see Eq. (62)], for several values of Γ_R/U with fixed ratio Γ_R/Γ_L, showing that AO becomes significant once W increases past T_K/b_0 (indicated by dashed vertical lines). The exponent Δ_{AO} increases linearly with W for $W \ll T_K/b_0$, and saturates to a maximal value of $\sqrt{2}$ [see Eq. (63)] for $W \gg T_K/b_0$. The corresponding values of Δ_{ch} [from Eq. (7)] are not shown but agree with Δ_{AO} with relative errors of a few percent.

D. Summary for PS without sensor

The results of this section can be summarized as follows. (i) The energy scale setting the width of PS is proportional to T_K. (ii) This can directly be attributed to AO; as shown in Fig. 9, the ground states of two configurations on opposite sides of the switching points exhibit strong AO when their level positions differ by more than T_K/b_0. Thus quantum fluctuations between them, induced by operators such as $\hat{Y}$ and $\hat{Y}^\dagger$, are strongly suppressed. (iii) For the present model, PS will always be continuous as a function of ε_d, because (for given U) T_K is nonzero for any fixed choice of Γ_L and Γ_R (although exponentially small), and AO ceases to be important ($\Delta_{AO} \simeq 0$) once ε_d comes within T_K/b_0 of the switching point. Conversely, however, it should now also be plausible that an essentially abrupt PS will be achievable if, by a suitable modification of the model, the degree of AO between the configurations (0,1) and (1,0) can be enhanced sufficiently to push T_K to zero even for finite Γ_L and Γ_R. As pointed out by GBG,[17,18] this can be achieved by adding a charge sensor, to which we turn next.

V. POPULATION SWITCHING WITH SENSOR

In this section, we study the effects of adding an electrostatically coupled charge sensor to the model of the previous section, as proposed by GBG,[17,18] and analyze how this enhances the effects of AO. In particular, we show that by increasing the sensor coupling strength (U_S), the effective Kondo temperature (T_K^S) can be driven to zero, implying that population switching becomes abrupt. A study of how additional leads increase the effects of AO for static quantities has recently been performed in similar context, involving a multilead IRLM.[30] Similarly, AO is also known to play an important role for a model of

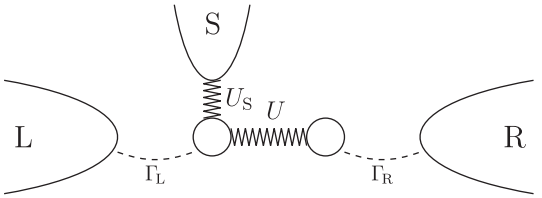

FIG. 10. Cartoon of the Hamiltonian (64), describing an asymmetric SIAM with an additional sensor lead coupled electrostatically to the left dot.

Ising-coupled Kondo impurities,[32,33] which can be mapped onto a model similar, though not identical, to that studied below.

A. Width of switching regime

GBG proposed to extend the asymmetric SIAM studied above by introducing a third lead as "charge sensor" for the left dot (see Fig. 10). For simplicity, it is taken to have the same density of states as the other two leads, but in contrast to the latter, it couples to the left dot only electrostatically (*not* by tunneling), with interaction strength U_S (with $\hat{c}_S \equiv \sum_\varepsilon \hat{c}_{\varepsilon S}$):

$$\hat{H} = \hat{H}_{\rm SIAM} + \sum_\varepsilon \varepsilon\, \hat{c}^\dagger_{\varepsilon S}\hat{c}_{\varepsilon S} + U_S \left(\hat{d}^\dagger_L \hat{d}_L - \frac{1}{2}\right)\left(\hat{c}^\dagger_S \hat{c}_S - \frac{1}{2}\right). \tag{64}$$

A plot of n_L and n_R as functions of ε_d for this model looks essentially similar to Fig. 7(b), showing population switching at $\varepsilon_d = -U/2$. However, when the strength of the coupling U_S is increased, the width of the PS, say W^S_{PS}, is strongly reduced below the value W_{PS} it had for $U_S = 0$, as predicted by GBG. This is illustrated in Fig. 11(a), which shows n_R (solid lines) and n_L (dashed lines) as functions of $(\varepsilon_d + U/2)/W_{PS}$, using a logarithmic scale to zoom in on the immediate vicinity of the PS. In fact, as U_S approaches a critical value U^*_S, the width W^S_{PS} drops exponentially towards zero, until it becomes too small to be resolved within double precision numerical accuracy.

The behavior of W^S_{PS} is mimicked by that of the Kondo temperature, calculated via the pseudospin susceptibility, $T^S_K \equiv 1/\chi_s$. We find that it decreases relative to its $U_S = 0$ value T_K, precisely in proportion to W^S_{PS}, such that

$$\frac{T^S_K}{T_K} = \frac{W^S_{PS}}{W_{PS}} \tag{65}$$

holds within our numerical accuracy.

The transition from a continuous to an abrupt PS as U_S crosses U^*_S has been predicted to be of the Kosterlitz-Thouless type.[17,18] This implies that T^S_K is expected to approach zero according to

$$-\ln T^S_K \sim (U^*_S - U_S)^\gamma\,, \tag{66}$$

where $\gamma = -1/2$. To test whether our data are conform to this expectation, Fig. 11(b) shows $\ln(T^S_K)/\ln(T_K)$ versus $(U^*_S - U)$ on a log-log plot. Indeed, we find a straight line for U_S not too close to U^*_S, consistent with Eq. (66). We extract the values $\gamma = -0.54 \pm 0.06$ and $U^*_S/U = 6.78 \pm 0.32$ by making linear fits over several somewhat different fitting ranges and taking the average and standard deviation of the fit parameters as final

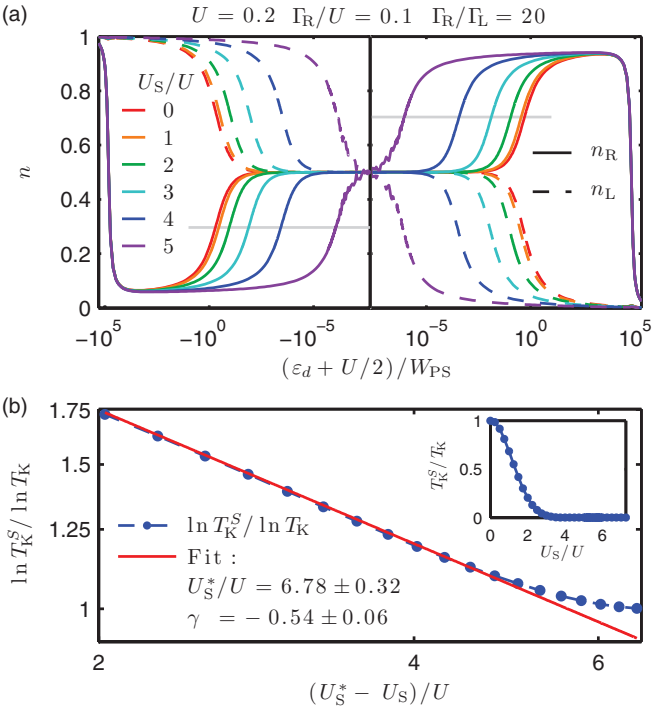

FIG. 11. (Color online) Population switching for the charge sensor model of Eq. (64). (a) $n_R(\varepsilon_d)$ (solid lines) and $n_L(\varepsilon_d)$ (dashed lines) for several values of U_S/U, plotted versus $(\varepsilon_d + U/2)/W_{PS}$ in a pseudologarithmic fashion ("pseudo" in that the x axis is plotted logarithmic with positive and negative values to the left and right of the switching point, respectively, represented by the vertical solid line). The horizontal light solid lines indicate the values of n_R which define the widths W^S_{PS} of the PS regimes. The noisy behavior of the curves for $U_S = 5U$ at small values of ε_d indicates that our analysis cannot resolve smaller values for ε_d as we are reaching the limits of double precision numerical accuracy. (b) Inset: T^S_K/T_K as a function of U_S/U, showing the rapid decrease of the Kondo temperature with increasing coupling. Main panel: $\ln T^S_K/\ln T_K$ versus $(U^*_S - U_S)/U$, plotted on a log-log scale (dashed line with dots), together with a linear fit using Eq. (66) (solid line).

fitting results. The relatively large errors of about 10% are a consequence of the fact that it is not possible to obtain data for U_S closer to U^*_S, since this would drive T^S_K below the level of numerical noise.

We note that analytical calculations based on Refs. 17 and 18 [using the more accurate criterion, $J_z(U^*_S) = J_{xy}(U^*_S)$ in the notation of these papers] predict the critical interaction to be $U^*_S/U \sim 7.6$. The agreement of this prediction with the numerical result of 6.8 is quite respectable, given the inaccuracies in both the numerical and analytical calculations [for the latter, inaccuracies arise since the cutoff scheme employed in the analytical calculation is different from the one realized numerically. The cutoff appears explicitly in the arguments of the functions Q in Eqs. (6) to (10) of Ref. 17].

Though the above results unambiguously show that the width of PS decreases exponentially as U_S approaches a critical value U^*_S, an analysis based purely on W^S_{PS} can not access the critical point itself or the regime beyond. We therefore proceed now with a numerical calculation of the dynamics of

the pseudospin-flip operator for which we are not constrained to $U_S < U_S^*$.

B. AO in dynamics of pseudospin-flip operator

The reason for the U_S dependence of W_{PS} and T_K^S is that the introduction of the sensor ($U_S \neq 0$) increases the influence of AO in the leads. As pointed out by GBG, the scaling dimension of $\hat{Y}$ acquires an extra contribution $\frac{1}{2}\Delta_S^2$ due to the sensor lead:

$$\eta_Y^S = \tfrac{1}{2}(\Delta_L + 1)^2 + \tfrac{1}{2}(-\Delta_R - 1)^2 + \tfrac{1}{2}\Delta_S^2 , \qquad (67)$$

where Δ_S is given by Eq. (42), with U_S replacing U. In analogy with Eq. (59),

$$T_K^S \simeq \omega_{he}\left(\frac{J_{xy}}{\omega_{he}}\right)^{1/(1-\eta_Y^S)} . \qquad (68)$$

By increasing U_S and thereby Δ_S^2, it is thus possible to drive η_Y^S beyond 1. This will render the pseudospin-flip operators $\hat{Y}$ and $\hat{Y}^\dagger$ *irrelevant*at the $J_{xy} = 0$ fixed point, thus suppressing quantum fluctuations between the (0,1) and (1,0) configurations, and, hence, pushing T_K^S down to zero.

To check this scenario explicitly, we have studied the U_S dependence of η_Y^S by extracting it from the spectral function $\mathcal{A}_Y^{eq}(\omega)$, calculated at the particle-hole symmetric point for several values of U_S. The general shape of $\mathcal{A}_Y^{eq}$, shown in Fig. 12(a), is similar to that of Fig. 8(a) for $U_S = 0$: for frequencies well below $\omega^* \simeq T_K^S$, $\mathcal{A}_Y^{eq}(\omega)$ scales as

$$\mathcal{A}_Y^{eq}(\omega) \sim \omega^3 , \quad \omega \ll \omega^* , \qquad (69)$$

while in the regime of intermediate frequencies, $\omega^* \lesssim \omega \lesssim \omega_{he}$ (cf. Sec. IV B), the spectrum shows AO power-law behavior,

$$\mathcal{A}_Y^{eq}(\omega) \sim \omega^{-1+2\eta_Y^S}, \quad \omega^* \lesssim \omega \lesssim \omega_{he} . \qquad (70)$$

Indeed, Fig. 12(b) shows that the values for η_Y^S extracted from the spectra (crosses) agree fairly well with those expected from Eq. (67). As before, deviations from pure AO behavior can be seen for $\omega \gtrsim \omega^*$. Moreover, for sufficiently large U_S/U, the exponents η_Y^S increase past 1, confirming that the pseudospin-flip operators become irrelevant. In that case the AO power-law behavior remains valid down to zero frequency, as shown in Fig. 12(c), since the scale T_K^S has been pushed to zero.

C. AO induced by quench of level positions

To further highlight the effect of AO on T_K^S, let us consider again the quench of level position [see Eq. (62)] studied in Sec. IV C, and repeat the analysis presented there, but now for several different values of U_S/U. Figure 13 shows the results for the exponent Δ_{AO}. For large values of W, the AO factor reaches its maximal value

$$\Delta_{AO}^{max} = \sqrt{(1)^2 + (1)^2 + \Delta_S^2} . \qquad (71)$$

This is similar to Eq. (63) for the model without sensor, but includes the additional contribution Δ_S^2 [given by Eq. (42), with U_S replacing U] from the displaced charge induced in the sensor lead by the change in local occupancy of the left dot from $n_L = 0$ to 1.

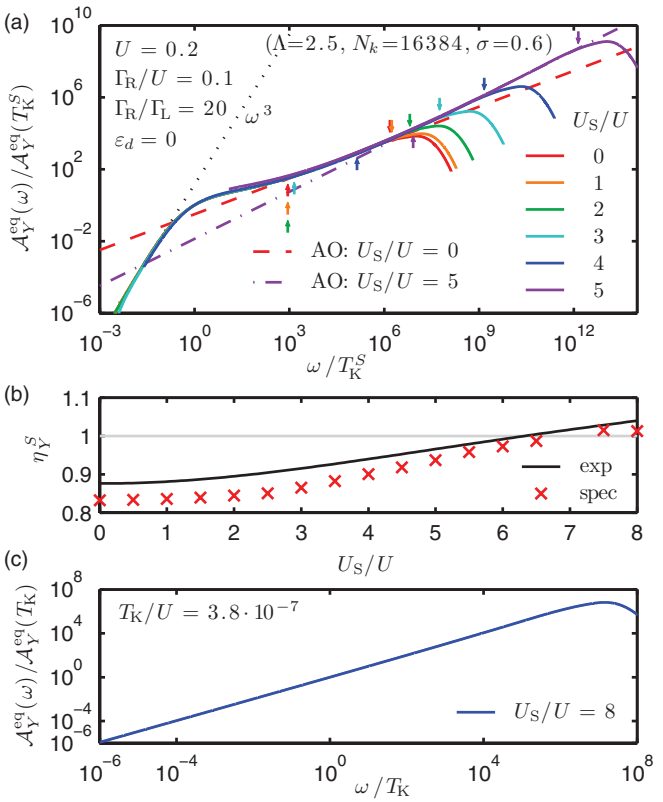

FIG. 12. (Color online) (a) The pseudospin-flip spectral function $\mathcal{A}_Y^{eq}(\omega)$ [cf. Eq. (58)] for the PS model with charge sensor, for several values of U_S/U, calculated at $\varepsilon_d = -U/2$: plotting $\mathcal{A}_Y^{eq}(\omega)/\mathcal{A}_Y^{eq}(T_K^S)$ vs ω/T_K^S yields a scaling collapse. The general shape of the curves is similar to those shown in Fig. 8: for $\omega < T_K^S$ we find Fermi-liquid behavior, $\sim\omega^3$ (dotted line), while for $\omega > T_K^S$, each curve shows a nontrivial AO power law, $\sim\omega^{-1+2\eta_Y^S}$ [cf. Eq. (61)], exemplified by the dashed and dash-dotted lines for $U_S/U = 0$ and 5, respectively. (b) Comparison of the values for η_Y^S expected from Eq. (67) (solid line), or extracted from power-law fits to the spectral function $\mathcal{A}_Y^{eq}(\omega)$ in the intermediate-frequency regime between T_K and the high-frequency maximum (crosses). Arrows in panel (a) indicate the fitting ranges, as in Fig. 8(a). The relative errors are below 5%, where the errors decrease with increasing U_S for similar reasons as in Fig. 8. The light horizontal line indicates $\eta_Y^S = 1$. (We were unable to obtain reliable data for U_S around $7U$, presumably because this is too close to U_S^*.) (c) $\mathcal{A}_Y^{eq}(\omega)/\mathcal{A}_Y^{eq}(T_K)$ vs ω/T_K for $U_S = 8U$. The AO power-law behavior $\omega^{-1+2\eta_Y^S}$ extends down to the smallest frequencies accessible, illustrating that the crossover scale T_K^S has become undetectable small.

The most important feature of Fig. 13 is the fact that the crossover scale T_K^S/b_0 (indicated by vertical dashed lines) is rapidly pushed to extremely small values as U_S/U is increased. Indeed, for $U_S = 8U$, which lies beyond the critical value of $U_S^*/U \simeq 6.78$ discussed above, Δ_{AO} is essentially pinned to its maximal value down to the smallest values of quench range W that we can access numerically. This is consistent with the fact that the corresponding spectral function $\mathcal{A}_Y^{eq}(\omega)$ at $U_S = 8U$, shown in Fig. 12(c), shows nontrivial AO power laws down to the lowest frequencies accessible, with no trace of a Fermi-liquid ω^3. This demonstrates very clearly, if somewhat indirectly, that the PS will be abrupt for $U_S > U_S^*$.

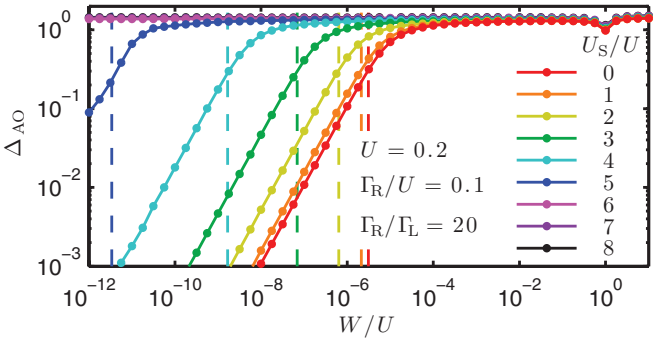

FIG. 13. (Color online) AO for the PS model with charge sensing. The exponent $\Delta_{\rm AO}$ [extracted from Eq. (1)] (solid lines with dots) is shown as function of quench size W/U [see Eq. (62)], for several values of $U_{\rm S}/U$, with fixed values of $\Gamma_{\rm R}$ and $\Gamma_{\rm L}$. We see that $T_{\rm K}^{\rm S}/b_0$ (indicated by dashed vertical lines) is pushed to zero as $U_{\rm S}$ increases past $U_{\rm S}^*/U \simeq 6.78$. Already for $U_{\rm S}/U \geqslant 6$, the curves are essentially indistinguishable, in that they do not deviate from their constant value for all W/U values accessible to our analysis. For $W \gg T_{\rm K}^{\rm S}/b_0$, the exponent $\Delta_{\rm AO}$ saturates to a maximal value given by Eq. (71). The corresponding values of $\Delta_{\rm ch}$ [from Eq. (7)] are not shown but agree with $\Delta_{\rm AO}$ with relative errors of a few percent.

D. Summary for PS with sensor

Let us summarize the results of this section, by way of extending the list of salient points collected in Sec. IV D. (iv) The presence of a charge sensor reduces the crossover scale $T_{\rm K}^{\rm S}$, which reaches zero at a critical coupling $U_{\rm S}^*$ [see Fig. 11]. (v) This reduction is due to the increased effect of AO in the leads, which increases the scaling dimension $\eta_Y^{\rm S}$ [see Fig. 12]; when the latter passes 1 (corresponding to $U_{\rm S} = U_{\rm S}^*$), the pseudospin-flip operators become irrelevant, hence J_{xy} flows to zero and $T_{\rm K}^{\rm S}$ vanishes, rendering the PS abrupt. (vi) Correspondingly, for $U_{\rm S} > U_{\rm S}^*$, the spectrum $\mathcal{A}_Y^{\rm eq}(\omega)$ shows nontrivial AO power-law behavior, $\omega^{-1+2\eta_Y^{\rm S}}$, all the way down to the smallest frequencies accessible [see Fig. 12(c)], and a low-frequency regime showing Fermi-liquid exponents does not exist.

VI. CONCLUDING REMARKS

The goal of this paper was to elucidate the role of the Anderson orthogonality catastrophe in giving rise to anomalous scaling dimensions in dynamical correlation functions for quantum impurity models. To this end, we have studied several setups involving (interacting) quantum dots and (noninteracting) leads. The quantum dots and leads may be interconnected electrostatically, or also through tunnel coupling. In our analysis, we focused on the asymptotic behaviour of various correlation functions $\mathcal{G}(t)$ and the corresponding spectral functions $\mathcal{A}(\omega)$ in the limit of long times or low frequencies, respectively. Their asymptotic behavior could be understood via a generalized version of Hopfield's rule, whose validity was checked and confirmed through an extensive NRG analysis. Our main result regarding the behavior of spectral functions in the different models considered are summarized in Table I. As a particular application, we performed a detailed study of population switching, both without and with a third lead that acts as a charge sensor. We confirmed a previous prediction[17,18] that when the charge sensor is sufficiently strongly coupled, population switching can turn into an abrupt quantum phase transition.

Aside from presenting a systematic discussion of the generalized Hopfield rule, which, hopefully, will be useful for practitioners in the fields, several general features have emerged from our analysis.

(1) In the context of a local quantum quench of type 1, where a change of parameters switches the Hamiltonian from $\hat{H}_{\rm i}$ to $\hat{H}_{\rm f}$, each lead-dot electrostatic coupling gives rise to an AO factor in the ground state overlap $|\langle G_{\rm i}|G_{\rm f}\rangle|$, reflecting a change in the many-body configuration of the lead when the charging state of the dot is modified. This AO factor scales as $N_\mu^{-\frac{1}{2}\Delta_\mu^2}$, where N_μ is the number of electrons in lead μ

TABLE I. Summary of our main results regarding the behavior of spectral functions $\mathcal{A}_Y^{\rm eq}(\omega)$ of the form Eq. (28), for those models considered in the present paper for which the Hamiltonian contains a hybridization operator connecting two dynamical sectors of the Hilbert space (hence the superscript "eq" on $\mathcal{A}_Y^{\rm eq}(\omega)$. The first two columns specify the section number, the model name, and a reference to the schematic diagram and the equation defining it). The hybridization gives rise to an energy scale ω^* (given in the third column by its name and a reference to the equation defining it) separating high from low-energy regimes. $\hat{Y}^\dagger \equiv \hat{C}^\dagger \hat{X}^\dagger$ is an operator that transfers the system between two dynamical sectors, and thus would lead to orthogonality catastrophe effects in the absence of hybridization. For $\omega \gg \omega^*$, the hybridization can be neglected in a first approximation and the spectral function displays AO behavior, $\mathcal{A}_Y^{\rm eq}(\omega) \sim \omega^{-1+2\eta_Y^0}$. In the low-frequency regime $\omega \ll \omega^*$, the hybridization is effectively strong, and simple Fermi-liquid behavior arises, $\mathcal{A}_Y^{\rm eq}(\omega) \sim \omega^{-1+2\eta_Y^{\rm eq}}$ with integer $2\eta_Y^{\rm eq}$. For each operator $\hat{Y}$ specified in the fourth column, the values of $\eta_Y^{\rm eq}$ and η_Y^0, together with a reference to the relevant equation, are given in columns five and six. The quantities $\Delta_d^{\rm ph}$, $\Delta_{\rm L}$, $\Delta_{\rm R}$, and $\Delta_{\rm S}$ occurring in column six are given by Eq. (42) with U replaced by U, $U_{\rm L}$, $U_{\rm R}$, and $U_{\rm S}$, respectively. It should be noted that more complicated behavior can occur for $\omega \gtrsim \omega^*$. In addition, ω^* can be zero if the hybridization operator is irrelevant, as may happen for the population switching system in the presence of a charge sensor, cf. V.

Sec.	Model	ω^*	$\hat{Y}$	$\eta_Y^{\rm eq}$	η_Y^0
III	Interacting resonant level, Fig. 3(a); (40)	$\Gamma_{\rm ren}$; (41)	$\hat{d}$	$\frac{1}{2}$;(43a)	$\frac{1}{2}(\Delta_d^{\rm ph})^2$; (44a)
			$\hat{d}\hat{c}$	2;(43b)	$\frac{1}{2}(\Delta_d^{\rm ph}-1)^2$; (44b)
			$\hat{d}\hat{c}^\dagger$	2;(43c)	$\frac{1}{2}(\Delta_d^{\rm ph}+1)^2$; (44c)
IV	Pop. switching, no sensor,Fig. 7(a);(51)	T_K;(57),(59)	$\hat{c}_L\hat{c}_R^\dagger\hat{d}_L^\dagger\hat{d}_R$	2;(60)	$\frac{1}{2}[(\Delta_{\rm L}+1)^2+(-\Delta_{\rm R}-1)^2]$; (61)
V	Pop. switching with sensor, Fig. 10; (64)	T_K^S; (68)	$\hat{c}_L\hat{c}_R^\dagger\hat{d}_L^\dagger\hat{d}_R$	2;(69)	$\frac{1}{2}[(\Delta_{\rm L}+1)^2+(-\Delta_{\rm R}-1)^2+(\Delta_{\rm S})^2]$; (70),(67)

and Δ_μ the change in the scattering phase, divided by π, in that lead. (AO factors from leads that are not interconnected by tunneling, so that the total charge within each channel is conserved, are multiplicative [see Eq. (31)].)[21]

(2) AO also arises for a type-2 quench, induced by an operator $\hat{X}^\dagger$ that connects initial and final ground states $|G_\mathrm{i}\rangle$ and $|G_\mathrm{f}\rangle$ lying in dynamically disconnected sectors of Hilbert space. In particular, AO influences the corresponding quench spectral function $\mathcal{A}_X(\omega)$, which scales as $\mathcal{A}_X(\omega) \sim \omega^{-1+\Delta_X^2}$ [see Eq. (27)]. For a Hamiltonian without tunnelling terms such as the LCM of Eq. (2), the spectral function for $\hat{X}^\dagger = \hat{d}^\dagger$ thus scales as $\mathcal{A}_d(\omega) \sim \omega^{-1+\Delta_d^2}$.

(3) When a type 2 quench has the form of a tunneling operator, $\hat{Y}^\dagger = \hat{c}\hat{d}^\dagger$, the asymptotic power law is modified to become $\mathcal{A}_{dc^\dagger} \sim \omega^{-1+(\Delta_d+1)^2}$ [see Eq. (39c)], implying a scaling dimension $\eta^0_{dc^\dagger} = \frac{1}{2}(\Delta_d+1)^2$. For a particle-hole symmetric interaction term [as in Eq. (40)], we have $-1 \leqslant \Delta_d \leqslant 0$ [see Eq. (42)], implying that $0 \leqslant \eta^0_{dc^\dagger} \leqslant 1/2$, thus tunneling between a dot and a single lead is always a relevant perturbation.

(4) The scaling exponent can be increased, and AO strengthened, by coupling the dot(s) to further leads. In particular, leads that couple to the dot only electrostatically (not via tunneling) contribute AO exponents of the form $\frac{1}{2}\Delta_\mu^2$, and thus enhance AO more strongly than leads that are tunnel coupled [cf. point (3)]. In this way, the scaling dimension of the tunneling operator can be increased past 1 [cf. Eq. (67)], and tunneling rendered irrelevant, making the no-hybridization fixed point attractive. In such a situation, population switching becomes a quantum phase transition, tuned by gate voltage.

(5) A particularly revealing way of demonstrating the effect of AO for population switching is to calculate the exponent Δ_{AO} for a type 1 quench in which the level position is abruptly changed from lying above to below the PS point [see Figs. 9 and 13, which are analogous to Fig. 6(a) for the IRLM].

(6) In the presence of tunneling terms of the form $(\hat{c}^\dagger\hat{d} + \hat{d}^\dagger\hat{c})$ (assuming these are relevant in the vicinity of the zero-tunnelling fixed point), operators such as $\hat{Y}^\dagger = \hat{d}^\dagger$, $\hat{c}\hat{d}^\dagger$, and $\hat{c}^\dagger\hat{d}^\dagger$ do not induce a quench, since they do not cause a switch between disconnected sectors of Hilbert space. Thus, when such an operator acts on the ground state, the resulting state will relax back to the ground state over long-time scales, say $t \gg 1/\omega^*$, where ω^* represents the local charge relaxation rate.

(7) The corresponding equilibrium spectral function $\mathcal{A}_Y^{\mathrm{eq}}(\omega)$ thus typically shows trivial Fermi-liquid exponents [e.g., Eq. (43)] in the regime of very small frequencies, $\delta E \lesssim \omega \ll \omega^*$, where the system is governed by a strong-hybridization fixed point. δE represents an infrared cutoff such as the level spacing in the lead. (Throughout this paper, we took $\delta E \simeq 0$, since in NRG calculations δE can be made arbitrarily small by using sufficiently long Wilson chains.)

(8) In an intermediate frequency regime $\omega > \omega^*$, the system is still in the vicinity of the zero tunneling fixed point, and the equilibrium spectral function $\mathcal{A}_Y^{\mathrm{eq}}(\omega)$ may contain signatures of anomalous AO exponents, scaling as $\omega^{-1+2\eta_Y^0}$ [e.g., Eq. (44)], where η_Y^0 represents the scaling dimension of $\hat{Y}$ calculated in the absence of tunneling. Thus such exponents may be extracted by focussing on this regime of intermediate frequencies [as done in Figs. 4, 8, and 12]. This is schematically indicated in Fig. 14(a). Near the lower end of this regime, i.e., for $\omega \gtrsim \omega^*$, deviations from the pure AO form may occur, since the tunneling term is effectively not small. This corresponds to the loss of validity of the lowest-order RG Eq. (23).

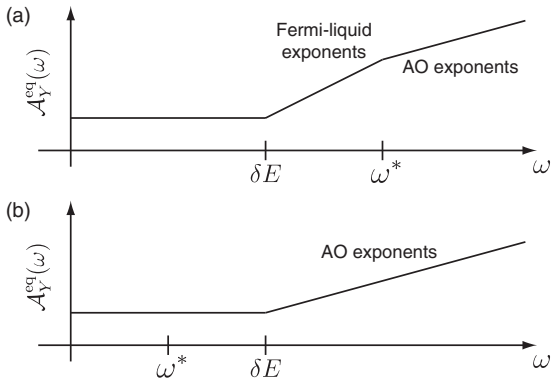

FIG. 14. Schematic depiction of the equilibrium spectral function $\mathcal{A}_Y^{\mathrm{eq}}(\omega)$ for the cases that the local charge relaxation rate ω^* is (a) larger or (b) smaller than the lead level spacing δE.

(9) If AO can be made so strong that the scaling dimension η_Y^0 of the operator $\hat{Y}^\dagger$ is larger than 1, the zero-tunnelling fixed point becomes attractive, the scale ω^* is pushed below δE (or, in the context of NRG, below the level of numerical noise). In this case, the regime of anomalous AO scaling $\omega^{-1+2\eta_Y^0}$ will extend all the way down to the smallest frequencies accessible [e.g., Fig. 12(c)], as schematically indicated in Fig. 14(b). In the transition region ($\eta_Y^0 \simeq 1$), the leading order term in the RG Eq. (23) is small and corrections to pure AO behavior will be important up to high frequencies. These include logarithmic factors typical of the isotropic Kondo problem.[25] While beyond the scope of this work, we believe the detailed behavior in this regime deserves further study.

To conclude, we note that cases where AO dominates in the low-frequency limit such that $\omega^* \simeq 0$, [as in point (9)], quantum fluctuations of the charge on the dot(s) are essentially completely frozen out. At zero temperature and in the absence of any extraneous decay mechanism, the system will remain localized in a particular local charge configuration. Thus varying the gate voltage in such a situation may lead to hysteretic behavior. It would be very interesting to experimentally search for such signatures of the freezing out of charge fluctuations by performing linear response measurements at the PS point.

ACKNOWLEDGMENTS

We thank R. Berkovits, L. Borda, Y. Imry, Y. Oreg, B. Sbierski, A. Schiller, G. Zaránd, and A. Zawadowski for helpful discussions. This work received support from the DFG (SFB 631, De-730/3-2, De-730/4-2, SFB-TR12, WE4819/1-1), in part from the NSF under Grant No. PHY05-51164, from the Israel-Russia MOST grant, the Israel Science Foundation, and the EU grant under the STREP program GEOMDISS. Financial support by the Excellence Cluster "Nanosystems Initiative Munich (NIM)" is gratefully acknowledged. M.G. is supported by the Adams Foundation of the Israel Academy of Sciences and Humanities, the Simons Foundation, the Fulbright Foundation, and the BIKURA (FIRST) program of the Israel Science Foundation.

APPENDIX: FIRMI-LIQUID SPECTRAL FUNCTIONS

In this Appendix, we study analytically the low energy ($\omega < \omega^*$) behavior of the spectral functions of the IRLM (SEE Sec. III B) and the PS setup (see Secs. IV B and V B). Let us start from the noninteracting resonant level [Eq. (40) with $U = 0$]. In that case, an elementary calculation gives for the retarded dot Green function,[53]

$$\mathcal{G}_d^R(\omega) = \frac{1}{\omega - \varepsilon_d - \frac{\Gamma}{\pi\rho}\mathcal{G}_c^{R,0}(\omega)} = \frac{1}{\omega - \varepsilon_d + i\Gamma}\,, \quad \text{(A1)}$$

where $\mathcal{G}_c^{R,0}$ is the retarded c Green function for $\Gamma = 0$, and we assumed the wide band limit (used just to simplify expressions, but actually not essential for any of the following arguments) $\mathcal{G}_c^{R,0}(\omega) = -i\pi\rho = -i\pi/2$ in units where $D = 1$. The imaginary part of the retarded Green function gives (up to a factor of $-1/\pi$) the well-known Lorentzian spectral function

$$\mathcal{A}_d^{\rm eq}(\omega) = \frac{1}{\pi}\frac{\Gamma}{(\omega - \varepsilon_d)^2 + \Gamma^2}\,. \quad \text{(A2)}$$

Thus, at low energies ($\omega \ll \Gamma$), $\mathcal{A}_d^{\rm eq}(\omega)$ becomes a constant, corresponding to $\eta_d^{\rm eq} = 1/2$ [which reproduces Eq. (43a)]. This behavior is easy to understand: in the absence of tunneling, $\mathcal{A}_c^{\rm eq,0}(\omega) = \rho$ is constant, reflecting the constant local density of states of the lead electrons near the end of the lead. In the presence of tunnelling, at low energy, the dot level is well hybridized with the lead, and assumes the role of the end of the lead, thus featuring the slowly-varying-low-energy spectral function $\mathcal{A}_d^{\rm eq}(\omega)$.

Based on similar arguments, one would expect that, in the presence of tunnelling, $\mathcal{A}_c^{\rm eq}(\omega)$ is still constant at low-energies, since in that limit the small spatial separation between the dot and the end of the lead should be unimportant. However, commensurability at half-filling (particle-hole symmetry) makes things bit more complicated. An explicit calculation gives

$$\begin{aligned}\mathcal{G}_c^R(\omega) &= \mathcal{G}_c^{R,0}(\omega) + \mathcal{G}_c^{R,0}(\omega)\sqrt{\frac{\Gamma}{\pi\rho}}\mathcal{G}_d^R(\omega)\sqrt{\frac{\Gamma}{\pi\rho}}\mathcal{G}_c^{R,0}(\omega)\\ &= -i\pi\rho\frac{\omega - \varepsilon_d}{\omega - \varepsilon_d + i\Gamma}\,. \quad \text{(A3)}\end{aligned}$$

Thus, when ε_d is nonzero, we indeed get a constant low-energy limit, i.e. $\eta_c^{\rm eq} = 1/2$. However, when $\varepsilon_d = 0$ (the value used throughout this paper for the IRLM), $\mathcal{G}_c^R(\omega) \sim \omega$ while $\mathcal{A}_c^{\rm eq}(\omega) \sim \omega^2$, corresponding to $\eta_c^{\rm eq} = 3/2$. To understand this behaviour, let us examine a half-infinite tight-binding chain with lattice spacing a and Hamiltonian $\hat{H}_{\rm TB} = \sum_{n=1}^{\infty}(\hat{\Psi}_{n+1}^\dagger\hat{\Psi}_n + \text{H.c.})$. Taking the continuum limit in the standard way, we can expand the fast-varying annihilation operators Ψ_n in terms of slowly varying (on the scale of the Fermi wavelength) right/left moving fields $\psi_{R/L}(x)$, with $x = na$:

$$\Psi_n = e^{ik_{\rm F}na}\psi_R(na) + e^{-ik_{\rm F}na}\psi_L(na)\,, \quad \text{(A4)}$$

where $k_{\rm F}$ is the Fermi wave vector. From the boundary condition $\Psi_0 = 0$, one gets $\psi_L(0) = -\psi_R(0)$, so we can define the single slowly varying field $\psi(x)$ by $\psi(x) = \psi_R(x)$ if $x > 0$ and $\psi(x) = -\psi_L(-x)$ if $x < 0$. Then,

$$\Psi_n = e^{ik_{\rm F}na}\psi(na) - e^{-ik_{\rm F}na}\psi(-na)\,. \quad \text{(A5)}$$

At half-filling, $k_{\rm F}a = \pi/2$, we get at the site next to the boundary

$$\Psi_{n=2} = -\psi(2a) + \psi(-2a) \sim -4a\partial_x\psi(0). \quad \text{(A6)}$$

The same thing happens at the *first site ($n = 1$) when we attach a dot, since at low energies, the dot behaves as the new first site*. The spatial derivative is equivalent to a time derivative, up to the Fermi velocity $v_{\rm F}$. This extra time derivative is responsible for the vanishing of the spectral function $\mathcal{A}_c^{\rm eq}(\omega)$ for $\omega \to 0$. Since we have derivative for both $\hat{c}$ and $\hat{c}^\dagger$ in the Green function and each gives an extra factor of ω, we end up with $\mathcal{A}_c^{\rm eq}(\omega) \sim \omega^2$. This behavior depends on being at half filling (particle-hole symmetry), hence is modified when ε_d is not zero.

Now we can discuss the higher spectral functions, $\mathcal{A}_{dc^\dagger}^{\rm eq}(\omega)$, and $\mathcal{A}_{dc}^{\rm eq}(\omega)$. These are the imaginary parts of the corresponding retarded Green functions, up to a factor of $-1/\pi$. The retarded Green functions are in turn the analytical continuation of the temperature Green functions to the real-frequency axis. And the temperature Green functions can be found in the noninteracting case using Wick's theorem.[53]

Performing these calculations for $\mathcal{A}_{dc^\dagger}^{\rm eq}(\omega)$, one gets

$$\begin{aligned}\mathcal{A}_{dc^\dagger}^{\rm eq}(\omega) = \frac{\rho}{\pi}\Im\Bigg[&\ln\frac{\omega - \varepsilon_d + i\Gamma}{-\varepsilon_d + i\Gamma}\\ &-\frac{\Gamma^2}{\omega(\omega + 2i\Gamma)}\ln\frac{\varepsilon_d^2 - (\omega + i\Gamma)^2}{\varepsilon_d^2 + \Gamma^2}\Bigg]\,. \quad \text{(A7)}\end{aligned}$$

Concentrating on $\omega \ll \Gamma$ one finds $\eta_{dc^\dagger}^{\rm eq} = \eta_c^{\rm eq} + \eta_d^{\rm eq} = 1$ for $\varepsilon_d \neq 0$ and $\eta_{dc^\dagger}^{\rm eq} = \eta_c^{\rm eq} + \eta_d^{\rm eq} = 2$ for $\varepsilon_d = 0$ [the data in Fig. 4(c) correspond to the latter case, which reproduces Eq. (43c)]. This simple summation of scaling dimensions is natural here, since there is only one possible different-time Wick pairing, of each single-particle operator with its conjugate.

For $\mathcal{A}_{dc}^{\rm eq}(\omega)$, however, there are two different-time Wick pairings, causing cancellations, and resulting in

$$\mathcal{A}_{dc}^{\rm eq}(\omega) = \frac{\rho}{\pi}\Im\left(\frac{\omega - 2\varepsilon_d + 2i\Gamma}{\omega - 2\varepsilon_d}\ln\frac{\omega - \varepsilon_d + i\Gamma}{-\varepsilon_d + i\Gamma}\right)\,. \quad \text{(A8)}$$

Concentrating again on $\omega \ll \Gamma$, one finds now that $\eta_{dc}^{\rm eq} = 2$ for *all* values of ε_d [which reproduces Eq. (43c)].[41] The reason is that in the low-energy continuum limit the product $\hat{d}\hat{c}$ becomes the product of annihilation operators at almost the same point. Hence, one should expand in the distance between $\hat{d}$ and $\hat{c}$ (lattice spacing). The leading term (with no spatial derivatives) vanishes by Pauli's principle; the next term involves a spatial derivative, leading to a factor of ω, similarly to the arguments above. Another factor of ω comes from the operator $\hat{c}^\dagger\hat{d}^\dagger$ appearing in the definition of $\mathcal{G}_{dc}^{\rm eq}(\omega)$. Thus, at low energies, we end up with $\mathcal{A}_{dc}^{\rm eq}(\omega) \sim \omega^3$ even for $\varepsilon_d \neq 0$. Although the above calculations were performed for the noninteracting case, the qualitative arguments explaining the low-energy behavior are valid even when $U > 0$. Moreover, since the system flows to the same strong-hybridization fixed point for all values of $U > 0$, the low-energy power laws are in any case *independent of U*. Our numerical results (see Fig. 4) are in agreement with this picture.

Let us now turn to the low-energy behavior of the PS setup in the case where PS is continuous. At low energy, the system is governed by Kondo physics, Eq. (53),[48–51] where the L-R degree of freedom plays the role of a pseudospin. The equivalence to Kondo continues to hold even in the presence of a charge sensor, as shown by GBG.[17,18] The operator $\hat{Y} = \hat{d}_R^\dagger \hat{d}_L \hat{c}_R \hat{c}_L^\dagger$ (which is relevant in the continuous-PS phase) is the pseudospin-flip local exchange term between the dot and the lead. Similarly, the IRLM is also equivalent to the Kondo model,[13,30,39] with the role of spin replaced by the charging state of the dot. The pseudospin local exchange term is simply $\hat{d}\hat{c}^\dagger$. Hence, when the parameters are properly mapped, the spectral functions $\mathcal{A}_Y^{\rm eq}(\omega)$ and $\mathcal{A}_{dc^\dagger}^{\rm eq}(\omega)$ are equivalent when the Kondo description applies (i.e., for $\omega \ll D$ for the IRLM, and $\omega \ll \omega_{\rm he}$ for the PS setup). In particular, $\mathcal{A}_Y^{\rm eq}(\omega)$ should exhibit an ω^3 behavior at low energy, similarly to $A_{dc^\dagger}^{\rm eq}(\omega)$ for $\varepsilon_d = 0$, as the NRG data shows [dotted line in Figs. 8(a) and 12(a)].

[1] P. W. Anderson, Phys. Rev. Lett. **18**, 1049 (1967).
[2] P. W. Anderson, Phys. Rev. **164**, 352 (1967).
[3] K. D. Schotte and U. Schotte, Phys. Rev. **185**, 509 (1969).
[4] G. D. Mahan, Phys. Rev. **163**, 612 (1967).
[5] J. J. Hopfield, Comments Solid State Phys. **2**, 40 (1969).
[6] B. Roulet, J. Gavoret, and P. Nozières, Phys. Rev. **178**, 1072 (1969); P. Nozières, J. Gavoret, and B. Roulet, *ibid.* **178**, 1084 (1969); P. Nozières and C. T. De Dominics, *ibid.* **178**, 1097 (1969).
[7] B. L. Altshuler and A. G. Aronov, JETP Lett. **30**, 482 (1979).
[8] V. L. Libero and L. N. Oliveira, Phys. Rev. Lett. **65**, 2042 (1990).
[9] A. O. Gogolin, Phys. Rev. Lett. **71**, 2995 (1993).
[10] N. V. Prokof'ev, Phys. Rev. B **49**, 2148 (1994).
[11] I. Affleck and A. W. W. Ludwig, J. Phys. A **27**, 5375 (1994).
[12] A. Furusaki, Phys. Rev. B **56**, 9352 (1997).
[13] A. O. Gogolin, A. A. Nersesyan, and A. M. Tsvelik, *Bosonization and Strongly Correlated Systems* (Cambridge University Press, Cambridge, 2004).
[14] R. W. Helmes, M. Sindel, L. Borda, and J. von Delft, Phys. Rev. B **72**, 125301 (2005).
[15] H. E. Türeci, M. Hanl, M. Claassen, A. Weichselbaum, T. Hecht, B. Braunecker, A. Govorov, L. Glazman, A. Imamoglu, and J. von Delft, Phys. Rev. Lett. **106**, 107402 (2011).
[16] C. Latta, F. Haupt, M. Hanl, A. Weichselbaum, M. Claassen, W. Wuester, P. Fallahi, S. Faelt, L. Glazman, J. von Delft, H. E. Türeci, and A. Imamoglu, Nature (London) **474**, 627 (2011).
[17] M. Goldstein, R. Berkovits, and Y. Gefen, Phys. Rev. Lett. **104**, 226805 (2010).
[18] M. Goldstein, Y. Gefen, and R. Berkovits, Phys. Rev. B **83**, 245112 (2011).
[19] K. G. Wilson, Rev. Mod. Phys. **47**, 773 (1975).
[20] R. Bulla, T. A. Costi, and T. Pruschke, Rev. Mod. Phys. **80**, 395 (2008).
[21] A. Weichselbaum, W. Münder, and J. von Delft, Phys. Rev. B **84**, 075137 (2011).
[22] J. Friedel, Phil. Mag. **43**, 153 (1952).
[23] J. Friedel, Can. J. Phys. **34**, 1190 (1956).
[24] D. C. Langreth, Phys. Rev. **150**, 516 (1966).
[25] A. C. Hewson, *The Kondo Problem to Heavy Fermions* (Cambridge University Press, Cambridge, 1993).
[26] Compare Ref. 22, p. 159; Ref. 23, Eq. (7); Ref. 24, Eq. (21); and Ref. 25, Sec. 1.2.
[27] O. Gunnarsson and K. Schönhammer, Phys. Rev. B **28**, 4315 (1983).
[28] J. Cardy, *Scaling and Renormalization in Statistical Physics* (Cambridge University Press, Cambridge, 1996).
[29] P. W. Anderson and G. Yuval, Phys. Rev. Lett. **23**, 89 (1969).
[30] L. Borda, A. Schiller, and A. Zawadowski, Phys. Rev. B **78**, 201301 (2008).
[31] T. A. Costi, P. Schmitteckert, J. Kroha, and P. Wölfle, Phys. Rev. Lett. **73**, 1275 (1994).
[32] N. Andrei, G. T. Zimanyi, and G. Schön, Phys. Rev. B **60**, 5125R (1999).
[33] M. Garst, S. Kehrein, T. Pruschke, A. Rosch, and M. Vojta, Phys. Rev. B **69**, 214413 (2004).
[34] L. N. Oliveira and J. W. Wilkins, Phys. Rev. B **24**, 4863 (1981); D. L. Cox, H. O. Frota, L. N. Oliveira, and J. W. Wilkins, *ibid.* **32**, 555 (1985).
[35] F. B. Anders and A. Schiller, Phys. Rev. Lett. **95**, 196801 (2005).
[36] F. B. Anders and A. Schiller, Phys. Rev. B **74**, 245113 (2006).
[37] R. Peters, T. Pruschke, and F. B. Anders, Phys. Rev. B **74**, 245114 (2006).
[38] A. Weichselbaum and J. von Delft, Phys. Rev. Lett. **99**, 076402 (2007).
[39] P. Schlottmann, Phys. Rev. B **22**, 622 (1980).
[40] M. Goldstein, Y. Weiss, and R. Berkovits, Europhys. Lett. **86**, 67012 (2009); Physica E **42**, 610 (2010).
[41] M. Goldstein and R. Berkovits, Phys. Rev. B **82**, 235315 (2010).
[42] G. Hackenbroich, W. D. Heiss, and H. A. Weidenmüller, Phys. Rev. Lett. **79**, 127 (1997).
[43] R. Baltin, Y. Gefen, G. Hackenbroich, and H. A. Weidenmüller, Eur. Phys. J. B **10**, 119 (1999).
[44] P. G. Silvestrov and Y. Imry, Phys. Rev. Lett. **85**, 2565 (2000).
[45] P. G. Silvestrov and Y. Imry, Phys. Rev. B **65**, 035309 (2001).
[46] D. I. Golosov and Y. Gefen, Phys. Rev. B **74**, 205316 (2006).
[47] C. Karrasch, T. Hecht, A. Weichselbaum, Y. Oreg, J. von Delft, and V. Meden, Phys. Rev. Lett. **98**, 186802 (2007).
[48] V. Kashcheyevs, A. Schiller, A. Aharony, and O. Entin-Wohlman, Phys. Rev. B **75**, 115313 (2007).
[49] H. W. Lee and S. Kim, Phys. Rev. Lett. **98**, 186805 (2007).
[50] P. G. Silvestrov and Y. Imry, Phys. Rev. B **75**, 115335 (2007).
[51] V. Kashcheyevs, C. Karrasch, T. Hecht, A. Weichselbaum, V. Meden, and A. Schiller, Phys. Rev. Lett. **102**, 136805 (2009).
[52] V. Meden and F. Marquardt, Phys. Rev. Lett. **96**, 146801 (2006).
[53] G. D. Mahan, *Many-Particle Physics* (Kluwer, New York, 2000).